

# {10 $\bar{1}2$ } twinning mechanism during *in situ* micro-tensile loading of pure Mg: Role of basal slip and twin-twin interactions

Nicolò M. Della Ventura<sup>a,\*</sup>, Szilvia Kalácska<sup>a</sup>, Daniele Casari<sup>a</sup>, Thomas E.J. Edwards<sup>a</sup>, Amit Sharma<sup>a</sup>, Johann Michler<sup>a</sup>, Roland Logé<sup>b</sup>, Xavier Maeder<sup>a</sup>

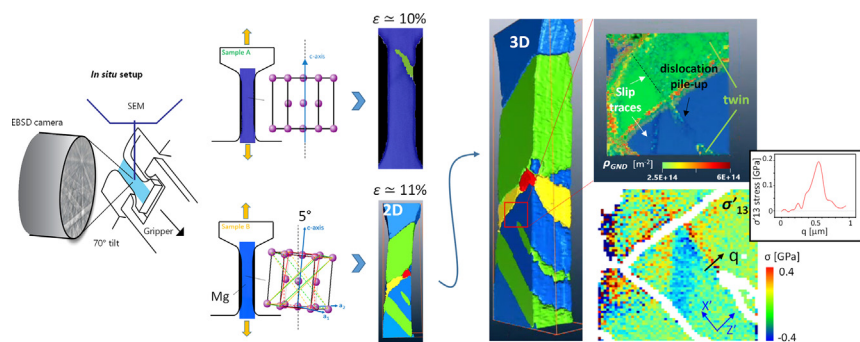
<sup>a</sup> Laboratory for Mechanics of Materials and Nanostructures, Swiss Federal Laboratories for Materials Science and Technology (Empa), 3602 Thun, Switzerland

<sup>b</sup> Laboratory of ThermoMechanical Metallurgy (LTM), PX Group Chair, Ecole Polytechnique Fédérale de Lausanne (EPFL), Rue de la Maladière 71b, 2000 Neuchâtel, Switzerland

## HIGHLIGHTS

- *In situ* HR-EBSD was used to map the sequence of events that occur during micro-tensile loading of single crystal Mg.
- Extension twins occur at the micron-scale when loaded off the c-axis, while limited twins form when loaded along the c-axis.
- The critical resolved shear stress for {10 $\bar{1}2$ } twinning has been determined to be ten times higher than in bulk material.
- Basal slip triggers {10 $\bar{1}2$ } twin nucleation and strongly favors twin growth and propagation.
- The 3D structure of the twins was obtained by FIB tomography and HR-EBSD allows associated stress and dislocations analyses.

## GRAPHICAL ABSTRACT



## ARTICLE INFO

### Article history:

Received 9 September 2020  
Received in revised form 29 September 2020  
Accepted 30 September 2020  
Available online 5 October 2020

### Keywords:

Magnesium  
*In situ* tension test  
Deformation twinning  
3D EBSD  
HR-EBSD

## ABSTRACT

An SEM *in situ* uniaxial tensile testing setup allowing HR-EBSD acquisition during deformation was used to study the extension twinning mechanism in magnesium (Mg) at the micron scale. Structures were fabricated with two different crystal orientations, respectively perfectly aligned with, and at 5° to, the [0001] axis. Limited {10 $\bar{1}2$ } twin formation was identified in the former case, while twinning was found to largely accommodate the plastic deformation in the latter case. These two different mechanisms are explained by the activation of basal slip when loading at 5° to the c-axis, which triggers {10 $\bar{1}2$ } twin nucleation and favors twin growth and propagation. The other orientation shows the activation of pyramidal slip together with only limited {10 $\bar{1}2$ } twin growth. The critical resolved shear stress for {10 $\bar{1}2$ } twinning has been determined to be ten times higher than in bulk material. 3D HR-EBSD mapping enabled reconstruction of the three dimensional twin structure after deformation. From this, the interaction between the dislocations located ahead of the incoming twin and a pre-existing twin boundary was investigated, where the GND distribution and the local shear stress were determined. The results show plastic accommodation up to ~11% of strain, revealing higher ductility than usually reported for bulk materials.

\* Corresponding author.

E-mail addresses: [nicolo.dellaventura@empa.ch](mailto:nicolo.dellaventura@empa.ch) (N.M. Della Ventura), [szilvia.kalacska@empa.ch](mailto:szilvia.kalacska@empa.ch) (S. Kalácska), [daniele.casari@empa.ch](mailto:daniele.casari@empa.ch) (D. Casari), [thomas.edwards@empa.ch](mailto:thomas.edwards@empa.ch) (T.E.J. Edwards), [amit.sharma@empa.ch](mailto:amit.sharma@empa.ch) (A. Sharma), [johann.michler@empa.ch](mailto:johann.michler@empa.ch) (J. Michler), [roland.loge@epfl.ch](mailto:roland.loge@epfl.ch) (R. Logé), [xavier.maeder@empa.ch](mailto:xavier.maeder@empa.ch) (X. Maeder).

## 1. Introduction

Known as the lightest structural metal, magnesium (Mg) and its alloys have attracted tremendous attention for weight reduction and increasing vehicle efficiency [1,2]. Unfortunately, this potential is curbed by limited ductility and machinability, due to the low number of favorable slip systems [3,4] and a plastic deformation mainly adapted by twinning mechanisms [5]. Mg is a hexagonal close packed (hcp) metal and the most common twinning mode is  $\{10\bar{1}2\} \langle 10\bar{1}1 \rangle$ , “extension twin”, characterized by a rotation around the *a*-axis (i.e.  $\langle 11\bar{2}0 \rangle$ ) of  $86.3^\circ$  from the matrix [6–10]. Useful improvements in ductility are observed by changing the critical resolved shear stress ( $\tau_{CRSS}$ ) for non-basal slip, which results in a change of the probability of twinning activities [8,11].

Twinning in hcp materials has been reported to exhibit size effect [12]. Indeed, it has been shown that due to the lack of precursor, the stress required to twin in hcp materials increases rapidly at smaller scales, favoring slip over twin formation [13–16]. Although the size effect also occurs for dislocation slip [17,18], in micron-scale structures multiple dislocation nucleation create pile-up arrays providing the energetic contribution *via* stress concentration required for twinning nucleation. In nano scaled samples, these arrays are less favorable as dislocations become mobile and their gliding accommodates deformation [14,19,20]. Therefore, it is assumed that a critical size exists below which twin appearance is suppressed [21,22]. In titanium, at room temperature and for strain rates in the order of  $1 \times 10^{-4} \text{ s}^{-1}$ , this value is found to be  $\sim 1 \mu\text{m}$  [14]. Pillar compression of pure Mg loaded along the  $[0001]$  axis with diameters from  $\sim 2$  to  $10 \mu\text{m}$  and strain rates from  $5 \times 10^{-4} \text{ s}^{-1}$  to  $1 \times 10^{-3} \text{ s}^{-1}$  also showed that plastic deformation was not [23] or in a very limited way [24] accommodated by twinning, suggesting twinning suppression at the micron scale. On the other hand, other studies on pure Mg with structure sizes ranging from  $0.4$  to  $20 \mu\text{m}$  in diameter, reported that plastic deformation is mainly adapted by  $\{10\bar{1}2\}$  twinning when micro-pillars are compressed along the  $[2\bar{1}10]$  axis [12,19,25]. In this case, the size effect was only associated with a stress increase for twin formation (smaller is stronger). This suggests that no intrinsic critical size exists for  $\{10\bar{1}2\}$  twinning formation and that the loading direction plays an important role in this mechanism.

Molecular Dynamics (MD) simulations report that the formation and glide of twinning dislocations (TDs) on the  $\{10\bar{1}2\}$  plane involves non-planar dissociations of slip dislocations [26–28]. Jeong et al. [12] showed that during  $[2\bar{1}10]$  compression of Mg, prismatic slip is activated (Schmid factor  $m = 0.43$ ) and the screw  $\langle a \rangle$  dislocations can cross-slip to the  $(0001)$  basal plane leading to twin formation. On the other hand, when loading along the  $[0001]$  axis, basal and prismatic slip are inhibited and  $\{10\bar{1}2\}$  twin suppression can be suspected. Nevertheless, additional computer simulations [29,30] showed that  $\{10\bar{1}2\}$  twins can also nucleate at the core of  $\langle c \rangle$  and  $\langle c + a \rangle$  dislocations under a sufficiently large applied shear strain. However, although the engineering stress-strain ( $\sigma$ - $\epsilon$ ) curves from Mg  $[0001]$  micro-compression experiments revealed significant strain hardening and traces of pyramidal slip on the deformed specimens [23,24], no significant twinning activity has been observed. In this context, it is important to point out that the Schmid factor on all the six  $\{10\bar{1}2\}$  planes during *c*-axis compression test is negative [31] and thus compression tests are not suitable for extension twin investigation. However, small extension twin formation reported in pillar compression can be related to the complex strain field at the pillar-punch contact, together with a bulging effect [32]. Tensile testing has the advantage to reduce the complexities related to several dimensional constraints [33] and additionally the

Schmid factor for the  $\{10\bar{1}2\}$  twin plane becomes close to the maximum during *c*-axis loading, making the investigation more reasonable.

Furthermore, the two-dimensional nature of simulations and experiments limits the investigation of several mechanisms. By simulations, it was seen that the atomic movement combined with the propagation of  $\langle 10\bar{1}1 \rangle$  TDs on  $\{10\bar{1}2\}$  planes lead to the growth of twins perpendicular to the twin plane [26,34–39]. Basal slip-twin boundaries interaction has also been reported to be important in twin propagation, but unfortunately, only a few experiments are present in literature to demonstrate that [28,40]. Also, the assessment of the three-dimensional growth of the twin and the characterization of its “dark side” (i.e. observation along the twinning shear direction) are difficult, but however necessary to get a global picture of the twin mechanism [34,41]. The “bright side” refers to the observation along a direction perpendicular to both the twinning shear direction and the normal to the twin plane. Additionally, twin-twin junctions frequently suggest the possibility of extension twins crossing process, i.e. twin-twin interpenetration, leading to debate whether the crossing mechanism is feasible or not [42–44]. Pei et al. [43] explain that the final result is an “apparent-crossing” domain, whereas Yu et al. [44] reported that this configuration is unfavorable, showing the need for detailed three-dimensional investigations. The possibility that a new twin of the same variant nucleates at the junction has also been considered [45].

The purpose of the present article is to investigate  $\{10\bar{1}2\}$  twinning formation in pure Mg during micro-tensile deformation of tensile bars (T-bars) with two different loading directions, respectively parallel and at  $5^\circ$  to the crystal *c*-axis. These two different orientations have been chosen to be able to study the influence of different slip systems on the twin nucleation and propagation processes. *In situ* high (angular) resolution electron backscatter diffraction (HR-EBSD) was used to map local stresses and the geometrically necessary dislocation (GND) density distribution at the surface of the T-bars during the nucleation and growth of  $\{10\bar{1}2\}$  twins [46–49]. *In situ* EBSD acquisition enables the analysis of the sequence of events that occur inside the gauge section during deformation. Post-mortem 3D HR-EBSD using focused ion beam (FIB) tomography was applied to measure the shape of twins, as well as the distribution of GNDs. The local residual shear stresses at the intersection of a growing twin and a pre-existing twin boundary (TB) have been analyzed in the reference frame associated with the activated twin variant (i.e. of the incoming twin).

## 2. Experimental procedure

### 2.1. Material

The materials used for this research are 99.999% pure single crystal Mg (0001), (PSC, Easton, USA) with an orientation accuracy of less than  $0.1^\circ$ , and 99.999% pure polycrystalline Mg (Goodfellow, UK). The two different pieces were mounted on SEM stubs for FIB milling and testing as shown in Fig. 1a. Sample A refers to the single crystal, while sample B is the polycrystalline specimen. In sample A, the *c*-axis of the crystal lattice inside the T-bars was aligned parallel to the loading direction ( $\phi_A = 0^\circ$ ) whereas, in sample B, the grain within which the structures have been created was characterized by a misalignment of ( $\phi_B = 5^\circ$ ) (Fig. 1b). The precise Euler angles (Bunge ZXZ' convention) referred to the global coordinate system (*X*, *Y*, *Z* in Fig. 1c) are ( $0^\circ 0^\circ 0^\circ$ ) for sample A and ( $355^\circ 358^\circ 0^\circ$ ) for sample B. On both materials, micro-T-bars with a cross section length of  $20 \mu\text{m}$  and cross sectional area of  $\sim 5 \times 8 \mu\text{m}^2$  have been fabricated (see Fig. 1c) by using FIB milling as explained in [50]. The junction radius was set to  $8 \mu\text{m}$  to limit stress

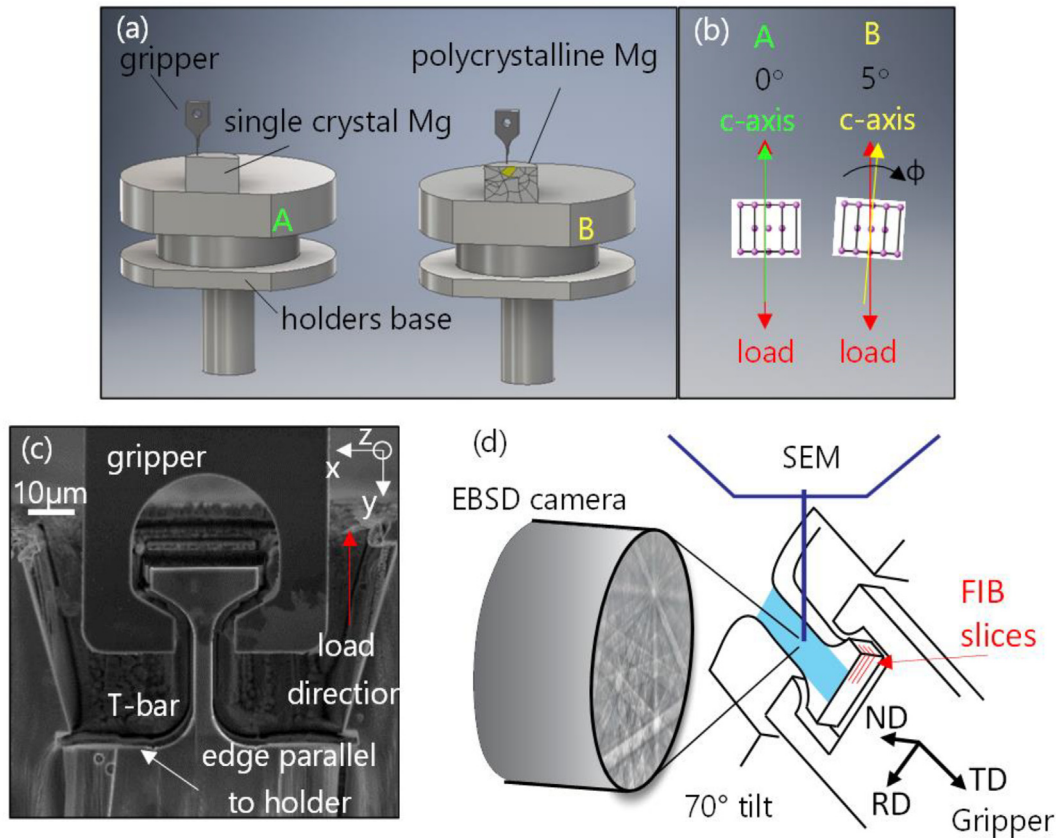


**Fig. 1.** *In situ* testing setup. (a) Single crystal (sample A) and polycrystalline Mg (sample B). (b) Loading direction according to the crystal c-axis for the two cases:  $\phi_A = 0^\circ$  and  $\phi_B = 5^\circ$ . (c) SEM image illustrating the gripper/T-bar structure before deformation and the global (sample) reference frame (X, Y, Z). (d) Schematic view of the *in situ* configuration inside the SEM chamber for micro-tensile testing concurrently with HR-EBSD acquisition.

concentrations at this site below 10%. The specimens had a taper angle  $\sim 1^\circ$  along the longitudinal direction and showed almost no curtaining artifact.

## 2.2. In situ experimental setup

The tests have been performed in a scanning electron microscope (SEM, Tescan Lyra) using an Alemnis nano-indenter system equipped with a nano-gripper [50] (Alemnis AG Switzerland) in displacement control at  $5 \times 10^{-4} \text{ s}^{-1}$  strain rate. The test ring has been adapted in order to be able to perform *in situ* HR-EBSD measurements at different strain increments, i.e. while the sample is under load, keeping the gripper displacement constant [46,51]. EBSD patterns were collected and recorded for off-line analyses with electron beam conditions of 20 kV and 15 nA, using an EDAX DigiView camera with  $2 \times 2$  binning ( $442 \times 442 \text{ px}^2$ ). The HR-EBSD cross-correlation was performed using the software CrossCourt V.4.3 (BLG Vantage, UK), with elastic constants of Mg (in GPa):  $C_{11} = 59.7$ ,  $C_{33} = 61.7$ ,  $C_{44} = 16.4$ ,  $C_{12} = 26.2$ ,  $C_{13} = 21.7$  [52]. The details about the HR-EBSD cross correlation technique can be found in [53–55]. Load drops in the  $\sigma$ - $\epsilon$  curves that coincide with EBSD map acquisitions are related to stress relaxation in the T-bars that occurs at the beginning of the displacement hold. This relaxation is due to some creep of the piezoelectric actuator and the load cell and possibly some minor stress relaxation in the material. Each *in situ* EBSD map was initiated after about 2 min, when this relaxation reached its minimal rate. Scanning was performed on the front surface of the deformed T-bars (Fig. 1d) with 150 nm step size. In total, 6 scans were recorded on the same surface during the *in situ* extension experiments: at  $\epsilon = 0$  (reference), in the elastic regime, then in the plastic regime at the first twin formation and proceeding higher strains up to  $\epsilon = 11\%$ . After

unloading and re-polishing the surface with FIB to remove carbon contamination due to recurrent scanning, the final map was acquired. Only structures with  $\phi_B = 5^\circ$  have been tested together with *in situ* HR-EBSD acquisitions since for those with  $\phi_A = 0^\circ$ , shadowing effect of the surrounding material could not allow *in situ* mapping.

## 2.3. Three dimensional HR-EBSD

Three-dimensional analysis of the shape and distribution of twins has been done for one T-bar loaded with  $5^\circ$  off the c-axis by using post-mortem 3D HR-EBSD together with FIB tomography in a static setup [56]. In this case, HR-EBSD measurements were acquired with a Symmetry detector and Aztec 4.1 software (Oxford Instrument, UK), with 20 kV and 10 nA beam conditions and 100 nm step size, using  $2 \times 2$  binning ( $622 \times 512 \text{ px}^2$ ). 2D HR-EBSD maps were captured after every FIB slice of 200 nm from the frontal surface throughout the thickness of the structure (Fig. 1d). FIB slicing was done at 30 kV 500 pA. After the HR-EBSD evaluation, Photoshop CC 2017 was used to manually align the slices by changing the visibility of one slice over the other. Amira v5.2 software was used to create the 3D reconstructions from the 2D maps. Transmission Electron Microscopy (TEM) analyses were not conducted as the samples have been consumed by FIB milling for 3D investigations and EBSD cross-section acquisitions.

## 3. Results

### 3.1. Schmid factor calculation

Fig. 2 shows the (0001) pole figure for both orientations. The chosen reference system for the hcp unit cell ( $a_1$ ,  $a_2$ ,  $c$ ) can be seen in Fig. 2a. All



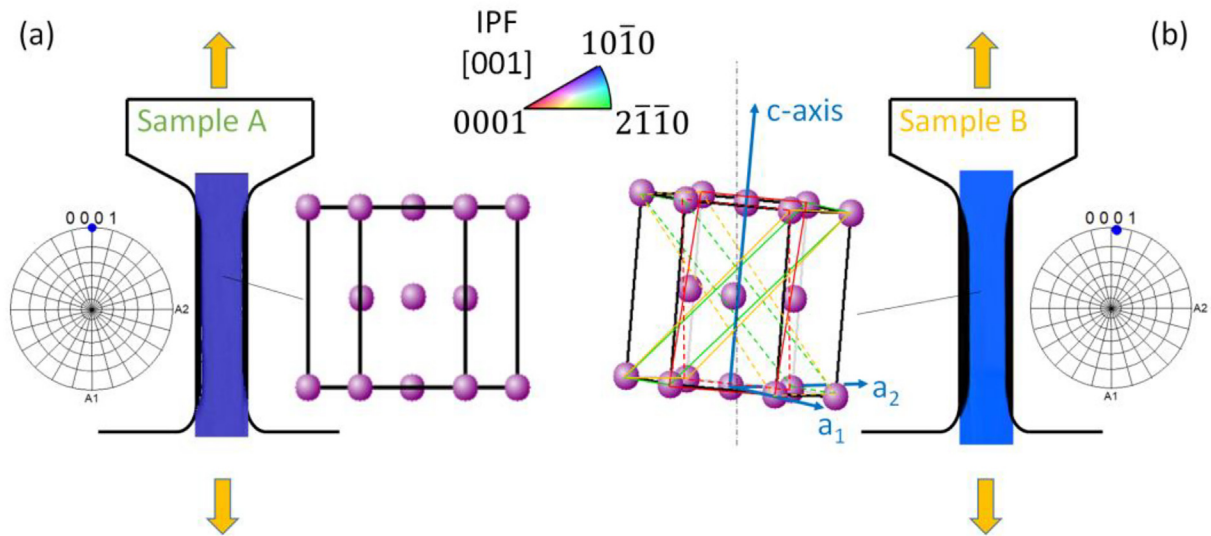


**Fig. 2.** Pole figures for the two different tested orientations showing the well-aligned c-axis/load direction for sample A (a), and the 5° in the case of sample B (b). The hcp coordinate system ( $a_1$ ,  $a_2$ ,  $c$ ) used in this work, together with all the {10 $\bar{1}2$ } twin variants, are shown in (b). Solid and dashed equally colored lines refer to conjugate variants.

six variants of the extension twin plane are also illustrated. Table 1 shows in detail the Schmid factor  $m$ ,  $\tau_{CRSS}$  and  $\sigma_y = \tau_{CRSS}/m$  (yield strength) values to predict the possible and preferred modes of deformation. In the case of  $\phi_A = 0^\circ$ , no basal slip activity is expected due to  $m = 0$ . The value of  $\tau_{CRSS}$  for the {10 $\bar{1}2$ } twin plane activation reported in literature for bulk Mg (~12 MPa, Table 1) suggests twin formation will occur in both loading directions, as the  $\tau_{CRSS}$  for prismatic and pyramidal 2nd order slip planes are much higher, i.e. 39–50 MPa and 80 MPa, respectively [57,58]. Concerning  $\phi_B = 5^\circ$ , basal slip activity can be expected due to a very low  $\tau_{CRSS}$  of ~1 MPa and a non-zero  $m$  value (see Table 1) [59,60].  $\sigma_y$  is given for comparison, pointing out the same order of magnitude between basal and twin deformation modes for this orientation. The  $\sigma_y$  values for the prismatic and pyramidal planes are expected to be at least 3 and 6 times higher, respectively, for both the  $\phi_A$  and  $\phi_B$  orientations.

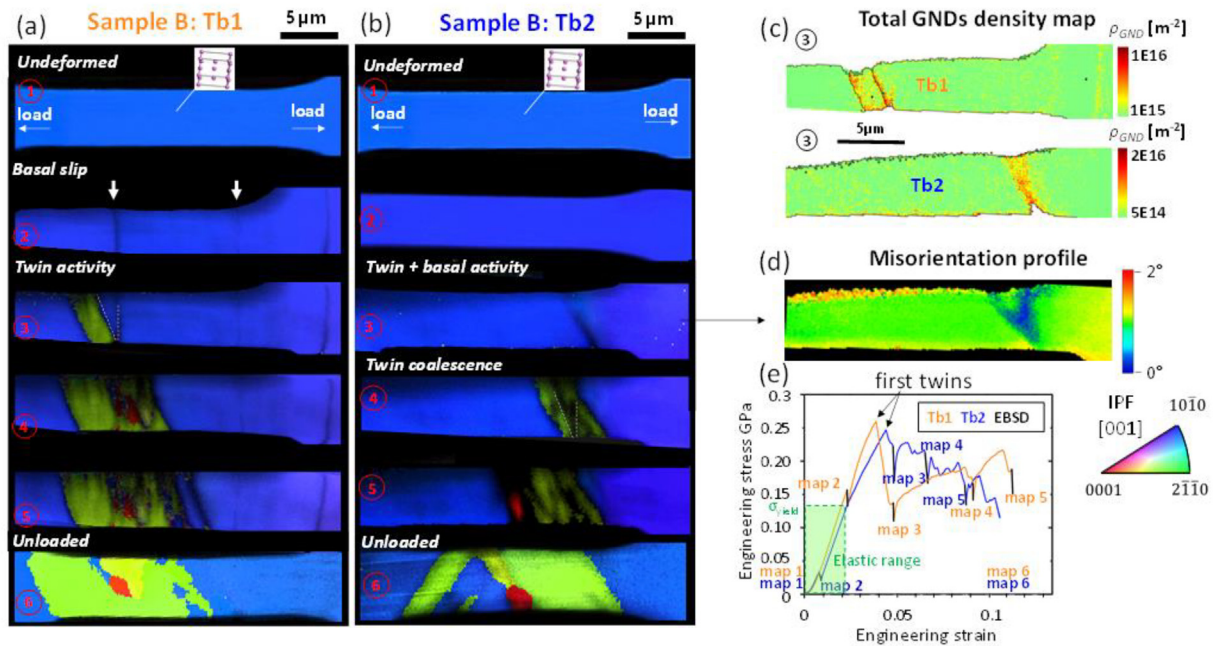
### 3.2. T-bars aligned at 5° to the c-axis. ( $\phi_B = 5^\circ$ )

Fig. 3a and b show the *in situ* crystal orientation maps (IPF color overlay) coupled with the image quality (IQ) maps (grayscale overlay) acquired during the tests for two similar T-bars, respectively called T-bar 1 (Tb1) and T-bar 2 (Tb2). The GND density distribution related

to the third intermediate load step after the first twin formation is shown for both samples in Fig. 3c. Fig. 3d illustrates the misorientation profile inside Tb2. The IPF color code in all maps indicates the crystal orientation in the out-of-plane direction. Numbers (1 to 6) indicate subsequent steps along the engineering  $\sigma$ - $\epsilon$  curve, as shown in Fig. 3e. The dislocations density of the pristine materials before the tests measured by HR-EBSD was detected to be in the order of  $10^{13} \text{ m}^{-2}$ . This value corresponds to the lower bound determination limit for GND density by HR-EBSD [53]. It has to be noted that statistically stored dislocations (SSD) cannot be detected with HR-EBSD. Concerning Tb1, the second map was captured at the onset of the plastic regime (~120 MPa) revealing that the initial micro-plasticity is accommodated at least in part by basal slip as evidenced by the lines of reduced Kikuchi pattern quality parallel to the trace of the basal plane on the sample surface. The degradation of Kikuchi pattern quality can be caused by local distortions of lattice planes within the diffracting volume that result from the storage of dislocations within a crystal during plastic deformation; pattern quality has previously been hence directly related to an equivalent plastic strain [61]. A slight change of slope on the engineering  $\sigma$ - $\epsilon$  curve trend can be seen (Fig. 3e) due to dislocation activation. For Tb2 (Fig. 3b) the second map has been taken in the very early elastic regime and no relevant differences emerged by comparing these first two EBSD

**Table 1**  
Schmid factor ( $m$ ),  $\tau_{CRSS}$  and  $\sigma_y$  of the slip and twin systems in bulk single crystal Mg for the two orientations considered.

Mode	crystal direction	plane	$\tau_{CRSS}$ (MPa)	$m$	$\sigma_y$ (MPa)	( $\phi_A = 0^\circ$ ) $m$	( $\phi_B = 5^\circ$ ) $\sigma_y$ (MPa)
Basal slip	[ $\bar{1}2\bar{1}0$ ]	(0001)	0.52–0.81 [59,60]	0.000	-	0.017	30.58–47.64
	[ $2\bar{1}\bar{1}0$ ]	(0001)				0.027	19.25–30.00
	[ $\bar{1}\bar{1}20$ ]	(0001)				0.070	7.42–11.57
{10 $\bar{1}2$ } Twin	[ $0\bar{1}1\bar{1}$ ]	( $0\bar{1}12$ )	12 [7]	0.499	24.04	0.485	24.74
	[ $10\bar{1}\bar{1}$ ]	( $10\bar{1}2$ )				0.500	
	[ $\bar{1}10\bar{1}$ ]	( $\bar{1}102$ )				0.500	
	[ $1\bar{1}0\bar{1}$ ]	( $1\bar{1}02$ )				0.495	
	[ $01\bar{1}\bar{1}$ ]	( $01\bar{1}2$ )				0.497	
	[ $\bar{1}01\bar{1}$ ]	( $\bar{1}012$ )				0.495	



**Fig. 3.** *In situ* EBSD coupled with IQ maps acquired for  $\sim 5 \mu\text{m}$  wide Mg T-bars loaded  $5^\circ$  off from the c-axis (sample B) at a strain rate of  $5 \times 10^{-4} \text{ s}^{-1}$ . (a) Initial, intermediate and final states for the 1st T-bar (Tb1) and (b) 2nd T-bar (Tb2) showing (i) twin nucleation at the junction with the activated basal slip (white arrows and dashed lines) and the free surface, (ii) progressive twin growth and (iii) multiple twin formation at higher strain values. The IPF color code refers to the out-of-plane crystal direction. (c) GND maps -color coded in logarithmic scale- after first twin events revealing high dislocation density along the  $(0\bar{1}12)$  twin and basal planes. (d) Tb2 misorientation gradient map of deformation step 3 highlighting basal plane activity where the twin nucleates. (e)  $\sigma$ - $\epsilon$  curve for both T-bars. Note that the stress and strain are nominal. The bold black load drops correspond to the location of the successive HR-EBSD maps.

maps. By continuing the loading, at  $\sim 268 \text{ MPa}$  and  $\sim 245 \text{ MPa}$  stress value ( $\sim 3.8\%$  and  $\sim 4.3\%$  strains, respectively), the nucleation of a  $(0\bar{1}12)$  twin is observed right after the onset of plasticity. This event is identified by comparing the maps of steps 2 and 3 (Fig. 3a and b). The formed twins appeared at the junction between activated basal planes and the surface of the sample. The rapid formations of twins are marked by load drops of  $\sim 142 \text{ MPa}$  and  $\sim 25 \text{ MPa}$ , similar to what was reported in [62]. Fig. 3a shows that the twin is already propagated through the entire width of the T-bar with a few micrometers thickness, whereas for Tb2, the twin is clearly thinner and less developed. This explains the smaller load drop observed in the  $\sigma$ - $\epsilon$  curve. GND density maps are reported in Fig. 3c underlining the high local density of dislocations along the basal and twin interfaces. In Fig. 3b step 3, no clear basal slip appears on the EBSD map, however its presence can be seen in the misorientation profile map (tolerance angle:  $2^\circ$ ; Fig. 3d), showing that the activated basal slip and twin planes are also clearly connected. Additional strain led to further thickening of the twin formed in Fig. 3a, linked with the irregular  $\sigma$ - $\epsilon$  trend recorded between the subsequent EBSD maps. In Tb2, the additional deformation led to the nucleation, propagation, thickening and coalescence of several twin embryos, as suggested by the band contrast inside the twin in the EBSD map (Fig. 3b step 4,  $\sim 6.4\%$  strain), indicated with a white inclined dashed line. At  $\sim 9\%$  of strain, the maps show a secondary twins appearance in both samples. Further elongations were performed until  $\sim 11\%$  of strain where the 5th map was taken just for Tb1. Due to surface contamination, the pattern quality was not sufficient to perform more *in situ* acquisitions. The tests have been carried out intentionally up to the same strain for both samples for comparison. The 6th maps, captured in unloading conditions after a few tens of nanometers of FIB polishing, highlight the presence of several twins. Concerning Tb2, additional twins have been detected in the 6th map that were not observed in the 5th map. This has to do with the additional loading that was performed before ending the test, where a few load drops occurred (Fig. 3e blue curve). Table A.1 (see Appendix A) summarizes the

different stages of deformation associated with the *in situ* EBSD acquisitions performed on Tb1 and Tb2.

### 3.2.1. Activated twin variants

Fig. 4 shows the pole figures for selected planes related to the grains in Tb2, while misorientation angles and rotation axes between different grains are listed in Table 2. The same results are found for Tb1 (not reported). The  $\{10\bar{1}2\}$  pole figure shows that the green, red and yellow IPF color twins are different variants of the same twin type. All of them have  $\sim 86.3^\circ$  misorientation with respect to the parent grain and a rotation axis that coincides with the a-axis of the hcp structure, typical for extension twinning. This is confirmed by the overlapping spots (circled) between the matrix (IPF color blue) and the different twins in the pole figures. In total, four variants have been detected:  $(\bar{1}012)$ ,  $(1\bar{1}02)$ ,  $(0\bar{1}12)$  and its conjugate  $(01\bar{1}2)$ . By analyzing the sequence of events through *in situ* HR-EBSD maps, it was observed that the  $(0\bar{1}12)$  green twin has been the first twin formed from the so-called "A" (parent) grain whereas the yellow  $(\bar{1}012)$  and red  $(1\bar{1}02)$  ones have been detected at a later stage of deformation. Colors and the coordinate system refer respectively to the chosen IPF and Fig. 2a. Table 2 shows also that the rotation axis between all the different twin variants is always along the  $\langle 10\bar{1}0 \rangle$  direction.

### 3.2.2. Post-mortem analysis

To assess the shape and spatial distribution of the twins, the 3D reconstruction of Tb2 has been performed (Fig. 5, see Supplementary material for Video 1, 2 and 3) in unloaded conditions. Fig. 5 shows the snapshots of the structure from different viewpoints around its longitudinal axis. The overall T-bar is illustrated in Fig. 5-I, whereas Fig. 5-II and 5-III show respectively the residual parent grains decoupled from the twinned ones and *vice versa*. The volumes of the twins and parent grains are reported in Table 3. Moreover, Fig. 6 shows the longitudinal EBSD cross sections made for both Tb1 and Tb2, where IPF and relative GND

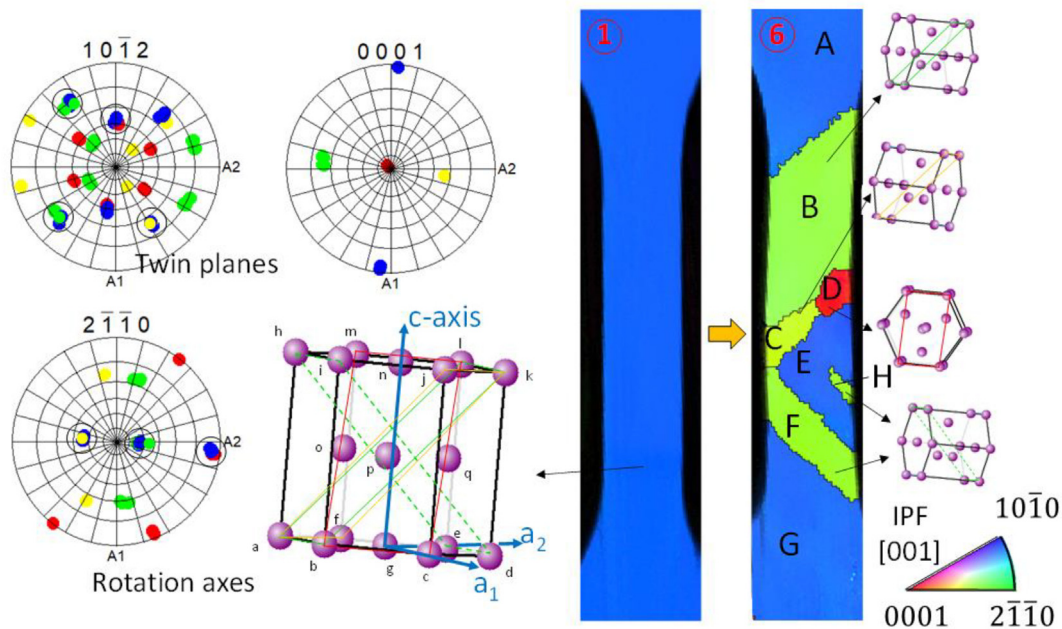


**Fig. 4.** Stereographic projections of  $\{10\bar{1}2\}$ ,  $\{2\bar{1}\bar{1}0\}$  and  $\{0001\}$  crystallographic planes for Tb2. Circled overlapping spots between green, yellow, red grains and blue (parent) along with the expected rotation axis confirm the extension twin formation of four different variants. 1<sup>st</sup> twin variant ( $0\bar{1}\bar{1}2$ ) -grain B- characterized by a twin plane that involves atoms  $a-b-k-l$ ; 2<sup>nd</sup> variant ( $01\bar{1}2$ ) -grain F- (conjugate of the 1st) atoms  $d-e-h-i$ ; 3<sup>rd</sup> ( $\bar{1}012$ ) -grain C- atoms  $a-f-k-j$ ; 4<sup>th</sup> ( $1\bar{1}02$ ) -grain D- atoms  $b-c-m-l$ .

maps taken at 2.4  $\mu\text{m}$  and 2.6  $\mu\text{m}$  from the front surface are shown. GND concentration can be found only inside the ( $0\bar{1}\bar{1}2$ ) twin related to Tb2 (Fig. 6b), in agreement with the mechanism explained in Section 4.1.1. Additionally, Fig. 6 shows that not all the twins propagated through the complete thickness of the structures, discussed later in Section 4.2. Dislocation accumulation ahead of the lenticular-shaped twin tip is further visible in Fig. 6b (blue arrow). In particular, to investigate the dislocation density in this region, Fig. 7a shows 15 of the 25 GND maps processed for Tb2, overlapped with the crystal orientation map in order to maintain the respective color of each grain (for the other maps see Supplementary material: Video 4). Fig. 6b, shows that pronounced GND density concentration occurred ahead of the lenticular-shaped twin tip along the ( $01\bar{1}2$ ) twin plane, which is discussed later in Section 4.3. Fig. 7b shows the misorientation profile inside the E grain. The stress field generated by the dislocation activity in this grain, referring to slice 13th, is reported in Fig. 7c and e, in the X-Y-Z global (sample) and X'-Y'-Z' local (associated with the ( $01\bar{1}2$ ) twin variant) reference frame (Fig. 7d), respectively. As twinning enables significant deformation of the lattice through crystal shear, the local shear stress is plotted (Fig. 7g), and discussed later in Section 4.4.

**Table 2**

Misorientations and rotation axis for the different grains inside Tb2. Letters (A-G) refer to Fig. 4.

Grains	Misorientations	Rotation axis
From B to A	85.7°	$[2\bar{1}\bar{1}0]$
From D to B	63.9°	$[10\bar{1}0]$
From C to B	57.4°	$[01\bar{1}0]$
From C to D	59.9°	$[0\bar{1}\bar{1}0]$
From E to C	87.1°	$[\bar{1}2\bar{1}0]$
From E to D	89.5°	$[11\bar{2}0]$
From F to E	86.1°	$[2\bar{1}\bar{1}0]$
From F to C	59.1°	$[01\bar{1}0]$
From G to F	86.0°	$[2\bar{1}\bar{1}0]$

### 3.3. T-bars aligned to the c-axis. ( $\phi_A = 0^\circ$ )

Two other similar T-bar structures, named T-bar 3 (Tb3) and T-bar 4 (Tb4) (Fig. 8), were loaded perfectly along the c-axis, to a similar total strain as for the other orientation. The EBSD maps captured before and after the test show the formation of only very small twins in both T-bars (Fig. 8a-c). Twin nucleation events are marked in the engineering  $\sigma$ - $\epsilon$  curve by arrows. The stress values at which the twins formed (i.e. between 248 and 255 MPa) are comparable with those reported in Fig. 3e for the other orientation. Concerning Tb3, two other twins are visible outside the strain gauge, near the contact with the gripper (Fig. 8a), and are related to the additional load drops reported in Fig. 8b. Contrary to what was observed for  $\phi_B$ , both structures show the nucleation of only one extension twin variant, which did not propagate through the entire gauge section length. Since all the tested structures have the same dimensions, these discrepancies can only be related to an orientation effect, as discussed later in Section 4.1.3. Strain hardening occurs after the first twin event. The additional load drops and irregularities on the  $\sigma$ - $\epsilon$  curve (Fig. 8b), not related to twin nucleation events, are likely due to slip activity necessary to accommodate the plastic deformation. The oblique dark lines in the T-bar gauge section suggest the activation of pyramidal slip during the deformation (Fig. 8c).

## 4. Discussion

### 4.1. Orientation effect on $\{10\bar{1}2\}$ twin nucleation and propagation mechanisms

#### 4.1.1. T-bars aligned at $5^\circ$ to the c-axis

Both T-bars loaded at  $5^\circ$  to the c-axis have shown similar twin nucleation locations corresponding to the intersection with the activated basal slip and the free standing surface, suggesting that the basal slip acted as a trigger mechanism for twin formation (Fig. 3c). The dislocation accumulation illustrated in the GND maps in Fig. 3c must be related to the multiple activated basal slip dislocations that can either glide out



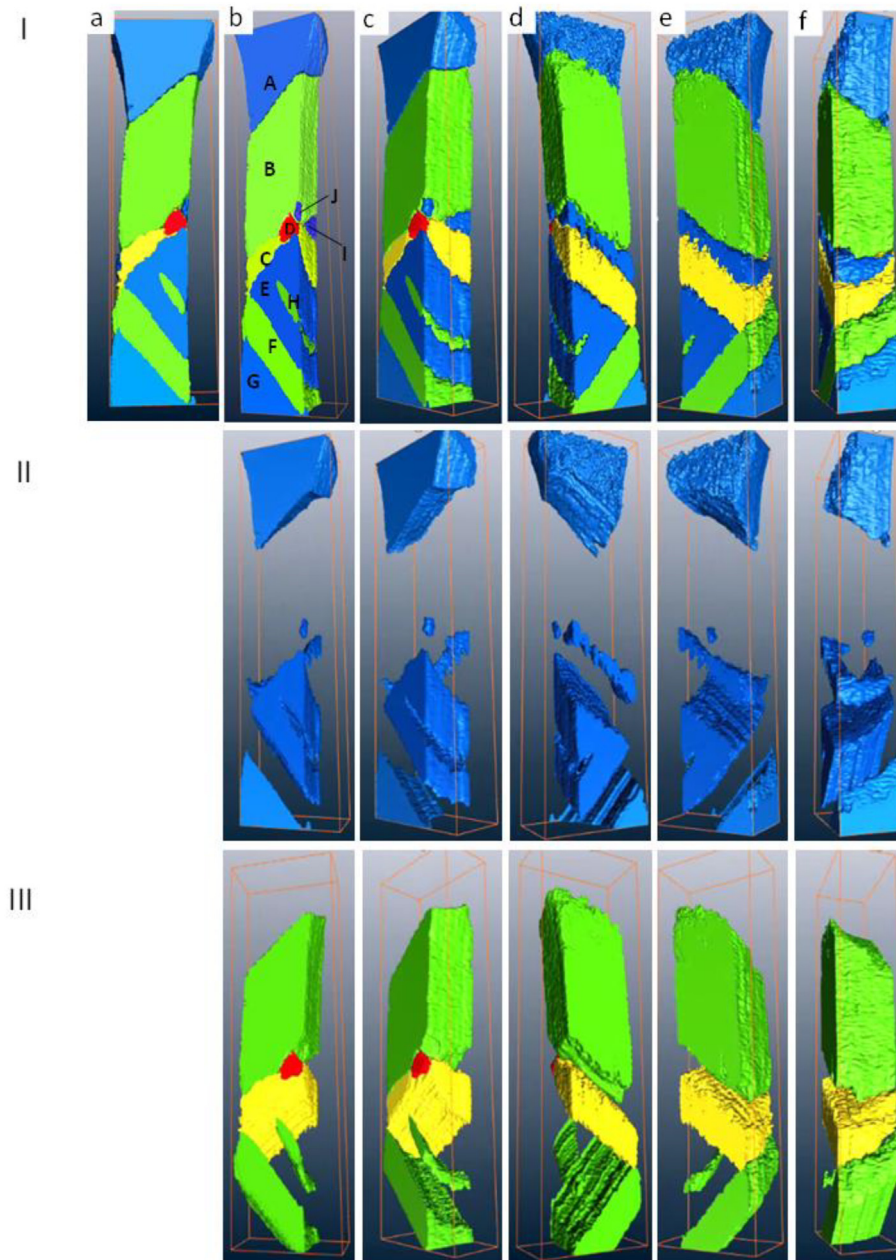


**Fig. 5.** Three-dimensional reconstruction of the T-bar from successive EBSD mapping and FIB milling. (a) EBSD map of Tb2 on the front surface; (b)–(f) 3D geometry of (I) parent and twins; (II) parent grain only; (III) twins only.

of the free surface creating a surface step or interact and pin leaving a good amount of dislocations inside the structure. Mendelson [63] and later Capolungo and Beyerlein [27] showed that the  $\langle a \rangle$  basal dislocation can dissociate into partial glissile TDs along the twin plane leading to twin nucleation. Also, the dislocation dissociation process has been recently observed in reported TEM experiments during the compression of pillars with an orientation that favors extension twin formation [12], triggering the twin nucleation. This

mechanism can therefore explain the extension twin formation in our case. After nucleation, the twin lamella expands quickly towards the whole structure leaving dislocations along the twin boundaries, as shown in the GND density maps (Fig. 3c). The interpretation of the twin nucleation and propagation mechanism from the successive EBSD maps is illustrated in Fig. 9 for the two T-bars, according to [27,39]. In Tb1, one single twin has formed in the gauge section (Fig. 3a and Fig. 9a–c), whereas the growth of two same-twin-

**Table 3**  
Volumes of the twinned and parent phases in Tb2. Letters (A–J) refer to Fig. 5–I–b.

Grain No.	A	B	C	D	E	F	G	H	I	J
Volume ( $\mu\text{m}^3$ )	179.24	340.66	84.64	1.02	112.02	90.75	43.6	5.72	11.47	0.44

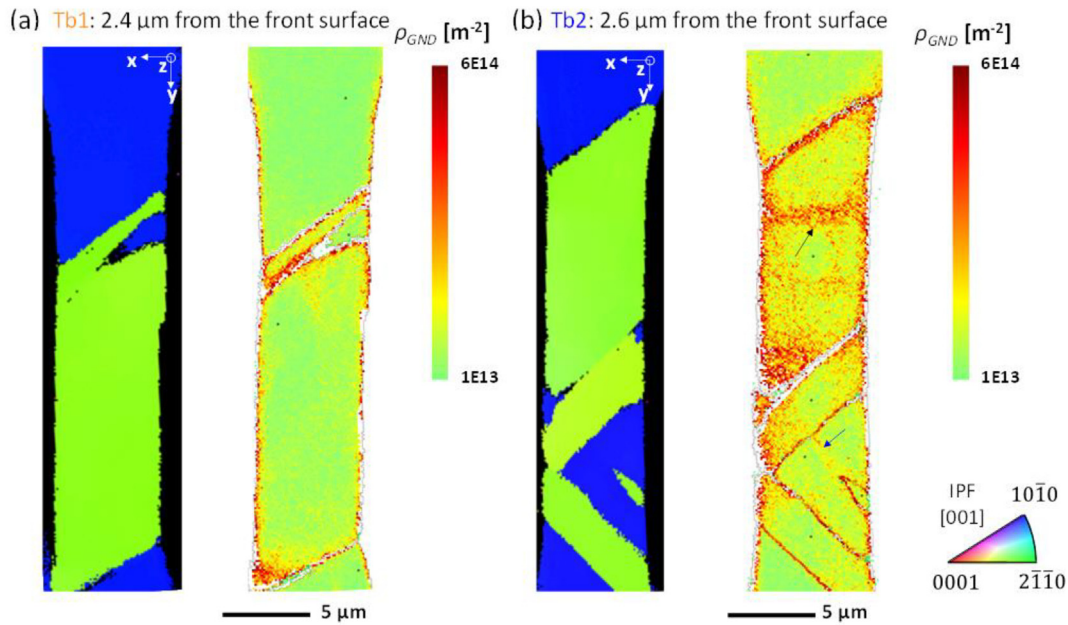


**Fig. 6.** Longitudinal cross-sectional EBSD maps of the deformed T-bars prepared by FIB and associated GND density distributions: (a) Tb1 maps at 2.4  $\mu\text{m}$  from the front surface; (b) Tb2 at 2.6  $\mu\text{m}$ . High GND density (black arrow) appears inside the developed (0 $\bar{1}$ 12) twin in Tb2 related to the basal slip that occurred in the matrix, associated with the second twin embryo formation process. Dislocation accumulation can also be seen ahead of the lenticular twin tip (blue arrow).

variant embryos characterizes the IPF green domain observed in Tb2 (Fig. 3b and Fig. 9d-f). The formation of the second (0 $\bar{1}$ 12) twin embryo can be linked to the second load drop at  $\sim 5.6\%$  strain, which is of similar magnitude to that of the (0 $\bar{1}$ 12) twin formed at 4.3% strain. These embryos expand into the upper crystal and eventually coalesce forming the larger detected (0 $\bar{1}$ 12) twin. To assess the strain energy density per T-bar unit volume ( $W$ ) up to the first twin event, a third order polynomial function was used to fit the  $\sigma$ - $\varepsilon$  curves discarding the load drops associated with the EBSD acquisitions. By calculating the integral of this function, it was found  $W_1 = 5.11 \times 10^6 \text{ J/m}^3$  and  $W_2 = 5.16 \times 10^6 \text{ J/m}^3$  for Tb1 and Tb2, respectively.

In Tb2, the second twin embryo nucleation mechanism appears to be similar to the first twin, triggered at the intersection of the basal slip (Fig. 9e). This can be seen in the 4th and 5th maps (Fig. 3b), where the detected IPF green twins show internal features (white vertical dashed arrow Fig. 3b) parallel to the basal plane, in the original matrix, that becomes prismatic in the twin domain. According to [40], when an existing twin interacts with an incoming basal slip plane, a basal edge dislocation can fully transform into prismatic through the gliding from the basal plane in the matrix onto the prismatic plane in the twin domain. For the screw component, the transformation is accomplished via multiple cross-slip events leading to a prismatic  $\langle a \rangle$  dislocations in the twin. However, a different scenario has to be depicted here where a mobile twin boundary moves by the glide of TDs on the twinning plane towards the stationary basal slip dislocations [64]. As reported in [64], when the TB meets the dislocation in the matrix, the  $\langle a \rangle$  dislocation transmutes into a different dislocation type that lies in a plane approximately parallel to the prismatic plane in the twin. According to Wang et al. [64]: “during further advancement of the TB, the transmuted dislocation may either move along with the TB or detach, leaving a fault in its wake”. The GND map from the longitudinal EBSD cross sections in Fig. 6 shows a high horizontal GND densification inside the twin related to Tb2 (black arrow in Fig. 6b) whereas no visible features appear inside the twinned region in Tb1 (Fig. 6a). This suggests that the activated basal dislocations that initiated the second twin

embryo nucleation in Tb2 result in a fault within the twin domain after the twin-slip interaction, as illustrated in Fig. 9.

The growth discrepancy between the twins in the two T-bars causes the different trends observed in the  $\sigma$ - $\varepsilon$  curves (Fig. 3e): Tb1 shows the usual hardening reported for twin formation, whereas Tb2 undergoes a softening behavior. Twin-slip interaction in Mg and alloys has been widely studied [35,40,65–69], especially in terms of how this interaction leads to hardening behavior [70–73]. Twin-slip interplay was found to be affected by the TB spacing and dislocation density mainly because TBs can act as a barrier to dislocation glide in the parent grain contributing therefore to hardening [74]. Additionally, since the TBs undergo a large amount of plastic deformation, multiple dislocations can become pinned or tangled leading to restrained dislocation motion, thus hardening [75]. This process has likely governed the mechanism inside Tb1. However, it is also known from the literature that applied forces cause relative motion across the boundary between two grains, leading to boundary sliding [76,77] and decreasing stress concentration during tensile loading, as experimentally observed in [78]. In Tb2, due to the higher presence of TBs, associated with the formation of multiple twin embryos, twin boundary sliding might have played a role, although not explicitly observed in our case. Konopka et al. [79] investigated *in situ* TEM the process of the generation of dislocations from TBs in copper and austenitic steel subjected to tension, where they concluded that an increase of the frequency of TBs results in a reduction of the flow stresses. Moreover, the nucleation and growth of multiple twin embryos are accompanied by several load drops, as experimentally seen, that contributes to an overall softening. Therefore, the significant softening observed in the  $\sigma$ - $\varepsilon$  response in Tb2 can be attributed to the high presence of twins that lead to profuse dislocation–TB reactions, twin coalescence and twin boundary migration related stress variation. To verify this, further experiments involving *in situ* TEM investigations and MD simulations detecting the particular dislocation mechanisms are required. Nevertheless, the opposite  $\sigma$ - $\varepsilon$  trends in Fig. 3e give a clear proof that, despite the same test conditions for Tb1 and Tb2, twinning growth mechanisms at the micron scale are highly stochastic and the multiple TB presence influences the stress response.



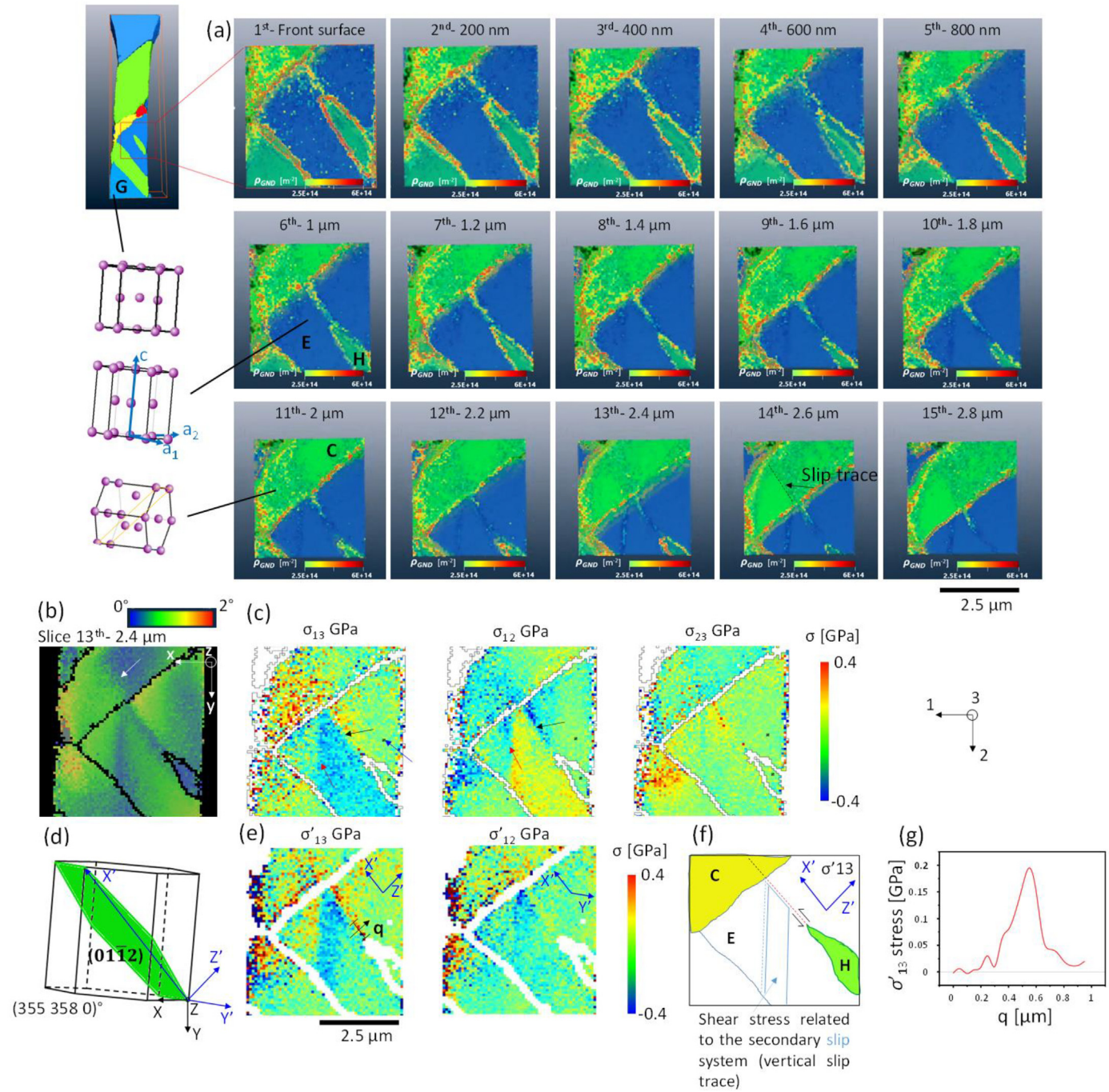


**Fig. 7.** GND maps, misorientations and shear stresses for the dislocation-twin boundary interaction inside the deformed Tb2. (a) 15 2D GND snapshots related to the red marked area for each 200 nm slice performed by FIB for three-dimensional reconstruction. (b) Misorientation profile map with tolerance angle of  $2^\circ$  of slice 13<sup>th</sup> (i.e. 2.4  $\mu\text{m}$  from the front surface). The white arrow indicates a marked misorientation inside the pre-existing twin. (c) Shear stress maps in GPa from HR-EBSD in the global reference frame, showing sign inversion across the twin plane (black arrows) along all the dislocation accumulation lines from the twin tip to the pre-existing twin boundary. Local higher stress concentration associated with activated slip systems (red arrows) is found vertically from the twin boundary into the E grain. The invariant plane of the active twin variant is indicated in green in (d) together with the sample (X, Y, Z) and the local (X', Y', Z') reference frames; X' along the twin shear direction and Z' normal to the  $(01\bar{1}2)$  twin plane. (e)  $\sigma'_{13}$  and  $\sigma'_{12}$  stress maps in the local reference frame. The reference point for HR-EBSD is marked by the blue arrow in (c). (f) Schematic representation of the dislocation-twin boundary interaction: red dashed line marking the direction of the accumulation of the dislocations ahead the incoming twin; blue and black dashed lines associated with the secondary activated slip systems respectively inside the E and C grains. (g) Residual  $\sigma'_{13}$  stress profile across the twin plane ahead of the lenticular twin showing a local increase of  $\sim 205$  MPa, resulting from averaging over 1  $\mu\text{m}$  length (e).

#### 4.1.2. T-bars aligned to the c-axis

When loading along the c-axis (sample A -  $\phi_A = 0^\circ$ ), basal and prismatic slip are inhibited. Pyramidal first order  $\langle c + a \rangle$  slip can be however activated, as it was demonstrated in terms of activation energy [80]. This is most likely the case in our deformed structures, shown by

the dark lines in the IQ map in Fig. 8c (black arrow) which are not associated with twinning. Moreover, MD simulation investigations on  $\{10\bar{1}2\}$  twins nucleating at the core of  $\langle c \rangle$  and  $\langle c + a \rangle$  dislocations showed that stable twin formation, via  $\langle c + a \rangle$  dislocation-assisted mechanisms, occurs at finite applied strain [29,30,81]. The trace of the

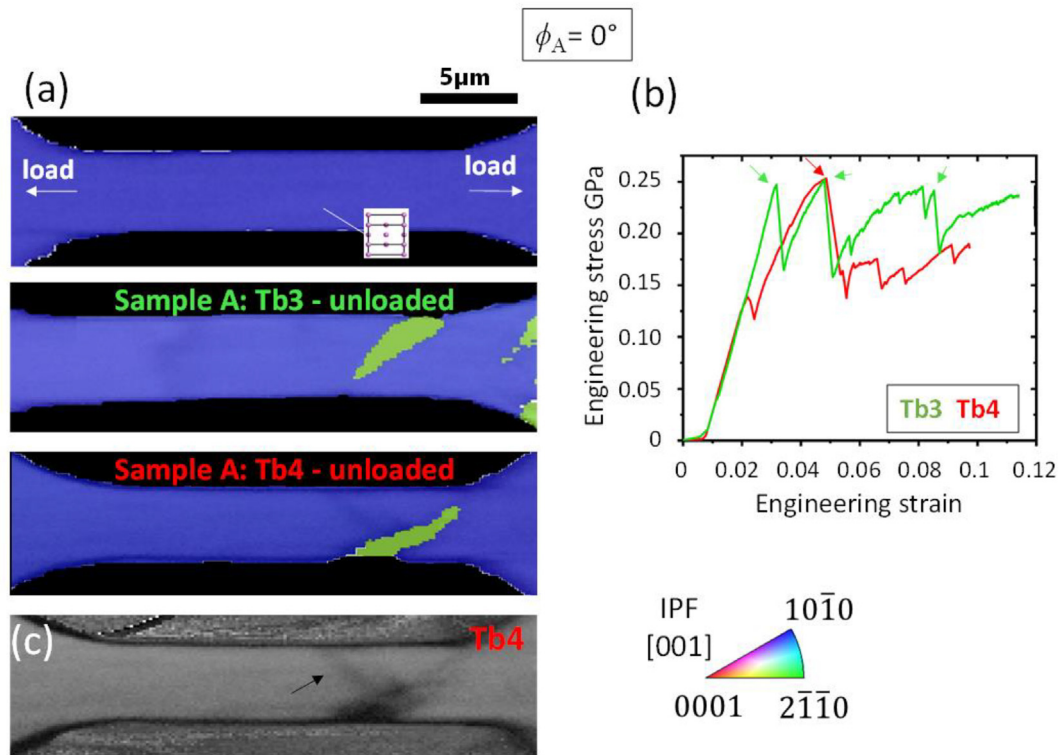


**Fig. 8.** EBSD maps of the deformed T-bars along the crystal  $c$ -axis (overlay of IPF and IQ maps). (a) Initial and final states showing formation of twins of the same variant in both structures (Tb3 in green; Tb4 in red). (b) Engineering  $\sigma$ - $\epsilon$  curve. Arrows indicate load drops associated with twin formation. (c) IQ map for Tb4 revealing darker features (black arrow) associated with pyramidal slip.

pyramidal slip intersecting the twin plane, shown in the EBSD map in Fig. 8c, suggests that such a scenario is possible for the  $\{10\bar{1}2\}$  twin nucleation mechanism in our case. Owing to the limited resolution of EBSD, Fig. 8c cannot prove rigorously that  $\langle c + a \rangle$  slip preceded the twin nucleation but provides an experimental basis for subsequent TEM works necessary to identify the dislocation type. However, important points can be raised from the observed twin propagation activity, as discussed in the following section.

#### 4.1.3. Role of the basal plane in $\{10\bar{1}2\}$ twin propagation

The presented experiments show an extensive propagation of different twin variants in the case of loading at  $5^\circ$  to the  $c$ -axis, where basal slip activities occur, and almost no twin propagation when basal slip is inhibited (*i.e.*  $\phi_A = 0^\circ$ ). Basal dislocations therefore also promote the twin propagation process. The dislocation-TB interaction in Mg has been analyzed extensively by MD simulations, particularly when basal dislocations meet a TB [82–85]. It has been shown that the dissociation

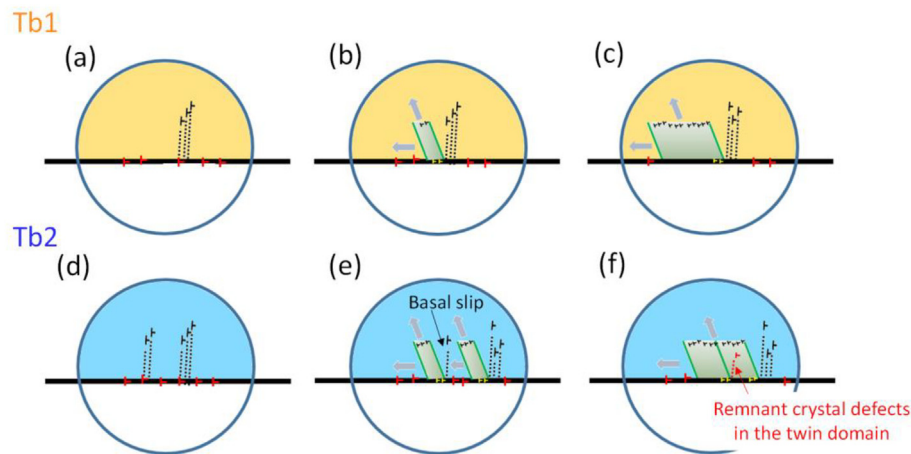


**Fig. 9.** Schematic representation of the formation and growth of  $(0\bar{1}12)$  twins for Tb1 (a-c) and Tb2 (d-f). (a, d) activated  $\langle a \rangle$  basal dislocations. (b, e)  $\langle a \rangle$  dislocation dissociation into twinning dislocation TDs (black upside-down Ts) and stair rod dislocations (yellow) according to [27,39], resulting in twin nucleation (green region) and subsequent growth (c, f). The red Ts represent the dislocations at the free surfaces mainly due to FIB milling. In the case of multiple same-variant twin formation as in Tb2 (f), embryos coalescence occurred leading to a larger embryo. Row of crystal defects consistent with basal dislocations transmutation related to the stationary slip-incoming TB interaction [64] is illustrated in (e-f).



of basal dislocations can generate multiple TDs at the  $\{10\bar{1}2\}$  TB [28]. In fact, Basal dislocation-TB interaction causes the absorption of the parent dislocation at the twin interface, leading to an interfacial step that acts as a source of TDs [86–88]. Fueled by the stress field of basal dislocations in the matrix, the TDs glide on the TB, producing TB migration [85]. This mechanism could therefore explain the promotion of twin propagation when the basal plane is activated. This also confirms the observations of Wang et al. [89], who have shown that during *in situ* tensile tests,  $\langle c + a \rangle$  pyramidal slip is favorable to nucleation but unfavorable to twin growth. Consequently, when twin migration is not eased by the presence of basal slip in the matrix, the nucleation of more twins or the activation of pyramidal slip systems are expected to be the mechanisms accommodating plastic deformation rather than twin growth. In other words, the initiation of other deformation systems would effectively accommodate the deformation requirement. Therefore, the suppression of the twins' thickening and propagation is primarily achieved by hindering TB motion, and in these experiments, basal slip absence was revealed clearly to be partly responsible for this suppression.

#### 4.2. $\tau_{CRSS}$ at the micron-scale

In this work, the complexities related to the presence of initial grain boundaries and incongruences between macroscopic and local stress are avoided until the first twin formation. The critical stresses associated with the onset of plastic deformation and  $\{10\bar{1}2\}$  twin nucleation can be thus determined from the  $\sigma$ - $\epsilon$  curves of all T-bars. Given the Schmid factor  $m$  from Table 1 for the first activated twin variants and the nucleation stresses from Fig. 3e and Fig. 8b, the range of the calculated  $\tau_{CRSS}$  for  $\{10\bar{1}2\}$  extension twin at the micron-scale is (118–124) MPa. These values are roughly ten times higher than those reported for bulk samples (Table 1) and can be explained by size effect [14,90].

#### 4.3. $\{10\bar{1}2\}$ twin-twin junction

As observed in Fig. 3, twin-twin junctions occurred inside the T-bars. By assessing the twin shape and distribution, the 3D reconstruction of Tb2 in Fig. 5 reveals that no twin-twin crossing mechanism occurred. This result is in agreement with Yu et al. [44] considering that, in the hcp unit cell, the twin crossing mechanism is unlikely because twinning is unidirectional having one set of TDs per twinning plane. Therefore, when loading favors the growth of two  $\{10\bar{1}2\}$  twin variants, one twin cannot transmit into the other across a TB, as confirmed here. Consequently, twin-twin boundary (TTB) intersection forms causing the generation of TTB dislocations that possibly lead to third twin variant nucleation. The intermediate EBSD maps taken for both T-bars tested at  $5^\circ$  to the  $c$ -axis show the systematic formation of the green, yellow and red IPF twins. The location of the latter is always detected at the intersection between the yellow (incoming) and green (pre-existing) twins. It appears from the 3D reconstruction that the red twin is constrained at the surface between these two twins in a highly strained region without the possibility of growing by crossing mechanism. This confirms what Kumar et al. suggested in [45]: an approaching  $\{10\bar{1}2\}$  twin that forms a twin-twin junction, would not likely transmit through an existing  $\{10\bar{1}2\}$  twin, but instead create a new twin of the same type. In this case, in both structures, the mechanism observed is:  $(0\bar{1}12) - (\bar{1}012) \rightarrow (\bar{1}\bar{1}02)$ . At the twin-twin junction, the TTB plane is defined as a common interface that separates two twins and its geometry can be curved to minimize interface energy [91–93], explaining the dissimilar interfaces between the red and yellow (and green) IPF-colored twins. Nevertheless, the misorientation and rotation axis relationship between the crystals remains unchanged. Except for the red IPF twin, it was observed from the 3D reconstruction that the twin-matrix interfaces globally follow the invariant-twin plane geometries (see also Fig. 4).

#### 4.4. Dislocation-TB interaction and 3D GND density map

As discussed earlier, the twin-twin junctions play an important role since the local shear strains induced by the incoming twin on the pre-existing one can be accommodated by other twin variant activation, possibly induced by the transformation of pre-existing dislocations. However, before the twins interact through their volume, the interaction between the dislocations ahead of a growing twin and a pre-existing twin boundary can lead to the activation of dislocation slip within or on the exit side of the pre-existing twin [94,95]. Fig. 5 shows that the lenticular-shaped green IPF colored twin (grain H) has propagated faster through the complete thickness of the T-bar compared to the longitudinal or transverse directions. It has been measured experimentally and supported by simulations that the growth of a finite twin domain that extends across a grain connecting opposite grain boundaries is limited by the surrounding constraints [96–99] (see also Section 4.4). The presented experiment illustrates indeed that the lenticular twin has not propagated until the boundary of the yellow IPF twin. The propagation ahead of the twin tip has been slowed down compared to the one along the structure's thickness. The explanation can be found by analyzing the 3D-GND map reconstruction. As illustrated in Fig. 7a, high GND density concentrates ahead of the lenticular twin tip and extends parallel to the habit twin plane towards the yellow TB. These dislocations are necessarily present to accommodate the crystal misfit induced by the highly strained region that arises from the local TD distribution located at the end of the lenticular twin tip. To characterize and identify the type of dislocations ahead of the twin tip, post-mortem HR-EBSD analysis is reported (Fig. 10). The HR-EBSD cross-correlation results show that through the 6 rotation gradients used to recover 33 dislocation types for Mg, only the  $\langle a \rangle$  edge type appeared significantly marked (Fig. 10a) as it fulfills the geometry of lattice rotation (i.e. spatial gradient of the rotation fields) associated with the high strain built at the end of twin H. Note that the direction of the Burgers vector refers to the hcp reference system adapted by the software (reported in Fig. 10b). Thus, negative values imply that the  $\langle a \rangle$  edge dislocations (black arrows Fig. 10a) point to the left. The nature of these dislocations can also be investigated by analyzing the Nye tensor components  $\alpha_{i3}$  (Fig. 10c–d) measurable through the HR-EBSD technique (see Appendix B). The  $\alpha_{i3}$  component calculation was done by a C++ program developed in-house [56]. Note that by the analysis of the Nye components the nature of each single dislocation cannot be assessed but rather the local results of their interactions. In Fig. 10d, only the  $\alpha_{i3}$  map shows remarkable GNDs concentration at the head of the twin tip (high red values indicated by the black arrow), i.e. associated with dislocations having Burgers vector projection along the  $x$ -axis (see Fig. 10c), referred to the (X, Y, Z) sample reference frame. The  $\alpha_{i3}$  components characterize therefore mainly  $\langle a \rangle$  edge type dislocations, confirming to what is reported in Fig. 10a. Since  $\langle a \rangle$  dislocations form at the twin tip during its propagation phase to accommodate the lattice deformation, when the Schmid factor is not null, the activation of micro-basal slip and their subsequent dissociation [28] may generate multiple TDs at the  $\{10\bar{1}2\}$  TB that fuel the growth process. On the other hand, in presence of the TB of twin C, the large atomic mismatch and the resulting lack of common slip planes between the different grains (H, C, E) lead to the detected dislocation pile-up (Fig. 7a) that limits the twin propagation by the exertion of back-stress on the approaching twin tip. The growth along the perpendicular direction is, however, not constrained by the presence of grain boundaries, which explains why the lenticular twin appears highly developed along the T-bar thickness (see Fig. 5–III). This indicates that the twinning growth mechanism shifts from an elongation-dominated process to a thickening-dominated process when crystal boundaries are present, as also suggested in [99].

So, one question remains open: how does the material respond to the stress concentration accumulated at the yellow TB in the location of the considered interaction? The discussed dislocation pile-up at the



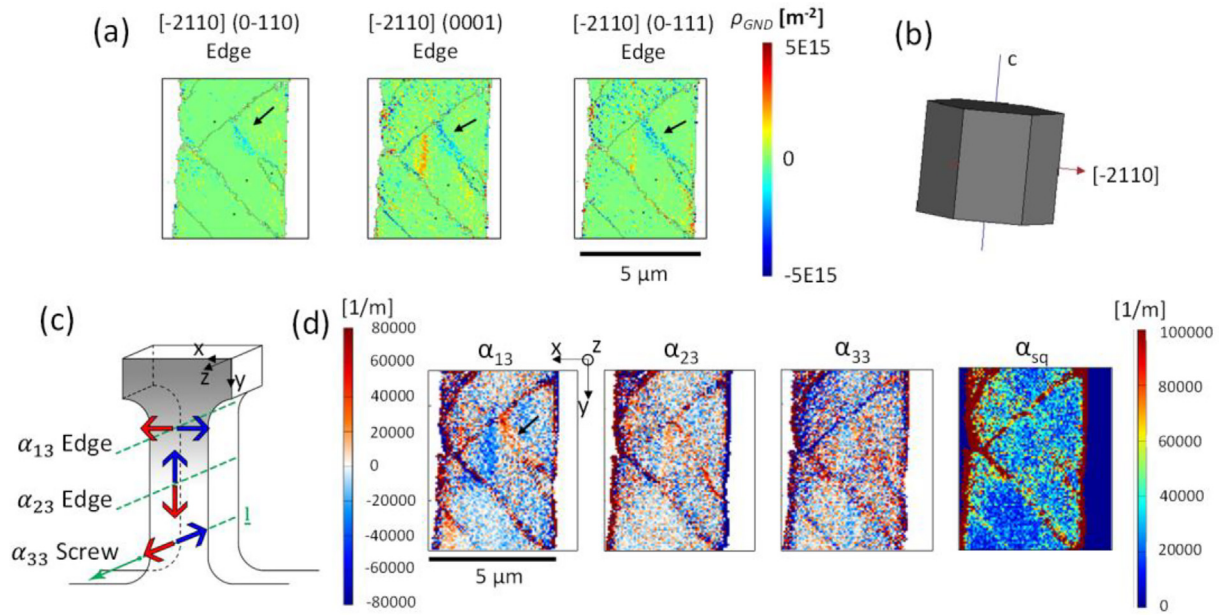


**Fig. 10.** (a) The three dislocation types with the same Burgers vector, measured via HR-EBSD post-processing, showing the greatest contribution in the location ahead of the twin tip. (b) Hcp reference system automatically adapted by the software. (c-d) Nye tensor analysis. (c)  $\alpha_{13}$  values legend related to the (X, Y, Z) global reference frame. An edge dislocation with Burgers vector pointing towards left (i.e. along x) appears red in the  $\alpha_{13}$  map (d). (d)  $\alpha_{13}$  and  $\alpha_{sq}$  values plotted for the 13<sup>th</sup> slice (2.4  $\mu\text{m}$  from the front surface) of the deformed Tb2. For a better understanding of the meaning of  $\alpha_{sq}$ , see Appendix B. Black arrow points out the elevated value of  $\alpha_{13}$  ahead of the lenticular-shaped twin tip associated with dislocation accumulation. No significant contribution seems to be given by  $\alpha_{23}$  and  $\alpha_{33}$  components.

boundary and the possible interaction with the TDs located at the TB of grain C seem to lead to the activation of secondary slip systems in the parent grain, likely related to prismatic slip, as shown from the vertical GND line inside the E grain in Fig. 7a, slice 13<sup>th</sup> at 2.4  $\mu\text{m}$  depth from the front surface. Thus, the high stress stored in the intersection has been subsequently adapted by the activation of secondary sets of dislocations. The dislocation piling-up seems to have therefore the important role of providing the energetic contribution needed to activate non-basal slip systems despite the relatively high  $\tau_{\text{CRSS}}$ . In this highly strained area, the crystal in E has experienced a distortion from the initial orientation as seen in Fig. 7b, where strong misorientation gradients are visible along both the (01 $\bar{1}2$ ) twin plane and the vertical axes where the GNDs are located. Moreover, the influence of the dislocations from the incoming (01 $\bar{1}2$ ) twin on the pre-existing ( $\bar{1}012$ ) is manifested through the change in the misorientation profile (Fig. 7b, white arrow) inside the latter. As illustrated in Fig. 7a (slice 14<sup>th</sup> at 2.6  $\mu\text{m}$ , black arrow), the pile-up of incoming  $\langle a \rangle$  dislocations impinging on a TB results also in the activation of dislocation slip inside the existing twin that has to be assessed as a shear accommodation process that partly relieves stress concentration.

Despite dislocation- and twin-twin boundary intersections are known to be areas of high residual stresses which can lead to crack nucleation [3,100], the tested structures have been deformed up to ~11% without cracking. This can be therefore due to the ability of the material to accommodate the local stresses (i) by the activation of secondary slip systems in the matrix and twin domains mainly within the vicinity of dislocation-TB regions and (ii) by the nucleation of other twin variants (as in grains B and C, Figs. 4 and 5), when further strain is imposed leading to twin-twin volume interaction (Section 4.2).

#### 4.5. Shear stresses

The local stresses are reported in Fig. 7c and e and have been measured by HR-EBSD. All the plotted shear stress magnitudes in Fig. 7 are referred to a reference point chosen in grain E, which is not stress free

(Fig. 7c, blue arrow), thus the stress component values are only relative. Note that the choice of the reference point does not affect the GND density, as the GND density is only related to local lattice curvatures [56]. The stress components  $\sigma_{13}$  and  $\sigma_{12}$  in Fig. 7c, mainly concentrated at the (01 $\bar{1}2$ ) twin tip, are found to change from positive to negative across the twin plane (see black arrows, Fig. 7c). To better interpret this polarity change, it is necessary to transform the stresses measured in the global (sample) coordinate system of Fig. 7c into a local one X'-Y'-Z' related to the active (01 $\bar{1}2$ ) twin variant (Fig. 7d). This allows the investigation of the stress components lying on the twin plane, associated hence with the twinning process. The local reference frame is defined in such a way that X' is along the twin shear direction and Z' is perpendicular to the twin invariant plane [51]. The stress fields of Fig. 7e in the local reference frame will be therefore  $\sigma'_{ij} = R\sigma_{ij}R^T$ , where R is the rotation matrix containing the unit vector components, expressed in the global reference frame, that are parallel to the twin shear direction, to the invariant plane normal, and their cross product, respectively. The plot of  $\sigma'_{13}$  (Fig. 7e), that is, the shear stress on the twin plane and along the twin shear direction, shows two significant contributions induced by (i) the dislocations motion along X' (red dashed line in Fig. 7f) and (ii) the secondary slip system activated at the yellow IPF-colored TB (blue dashed line Fig. 7f). The former, (i), is concentrated ahead of the twin tip towards the shear direction and its magnitude is higher than near the twin-parent interface. The stress field associated with  $\sigma'_{12}$  is instead mainly marked at the TB of twin C rather than in front of the twin H. As shown in Fig. 7e, the shear stress component  $\sigma'_{12}$  has no visible changes in polarity across the twinning plane and hence does not contribute significantly to the twinning deformation process. In contrast,  $\sigma_{13}$  and  $\sigma_{12}$  (i.e. in the global reference frame) show sign changes since they are partially constituted by the vector decomposition of  $\sigma'_{13}$ . The pile-up of the dislocations ahead of the lenticular shaped-twin induces a local increase of the  $\sigma'_{13}$  of ~205 MPa across the (01 $\bar{1}2$ ) plane (Fig. 7e); this is seen, Fig. 7g, in the average stress profile measured over a micron of length from the twin tip. As observed, the local stress variations ahead of the twin tip do not disappear upon

unloading, as reported also by crystal plasticity finite element (CPFE) simulations [99]. However, despite the positive shear value at the end of the twin tip provides a favorable condition for twin propagation, the lenticular twin did not reach the TB. In general, the growth and propagation of the twin within the parent grain are possible under applied load if the positive shear stress resolved on the twin plane and along the twin direction is sufficiently high to overcome the opposite stress (back-stress) induced by the parent domain surrounding the twin [101]. However, in presence of TB along the twin growth path, an additional back-stress contribution induced by the internal constraints imposed by the neighboring grains has to be accounted. Consequently, the increase in the flow stress with strain, necessary to promote further lengthwise twin propagation, is related to the increasing back-stress attributed to the dislocation-TB interference (*i.e.* pile-up), forcing the activation of other slip systems to accommodate the deformation requirements (Section 4.3). The region of residual shear stress in Fig. 7e (highlighted by solid blue lines in Fig. 7f) is indeed associated with the remnant incompatibility of the prior activated secondary slip system (ii), which operated in response to the local constraints induced by the TB to the approaching twin. Over the grain boundary, the stress field changes visibly as the different crystal orientation in the neighboring grain has a significant effect.

## 5. Conclusions

In the present work, an SEM *in situ* uniaxial micro-tensile testing setup was designed to perform HR-EBSD during deformation at the micron scale. This setup was used to study the extension twinning mechanism in pure Mg for two different crystallographic orientations, respectively along and at 5° to the c-axis. The following conclusions can be drawn from these experiments:

- {10 $\bar{1}$ 2} extension twinning was found to occur at the micron scale during tensile tests in Mg loaded along and at 5° to the c-axis, respectively. However, the nucleation and propagation mechanisms of the twins strongly differ between the two loading directions:

  - (1) For structures loaded at 5° to the c-axis, {10 $\bar{1}$ 2} twinning is triggered by the activation of basal planes. The latter appears to also strongly favor twin propagation/thickening processes, and to promote the formation of several twin variants in the strain gauge.
  - (2) On the contrary, the structures loaded perfectly parallel to the crystal c-axis show only single {10 $\bar{1}$ 2} twin nucleation with limited propagation. In this case, basal slip cannot be activated and {10 $\bar{1}$ 2} twinning is accompanied by the activation of pyramidal slip.

- The  $\tau_{CRSS}$  for {10 $\bar{1}$ 2} twin plane at the micron-scale is found to be ~120 MPa, *i.e.* ten times higher than the one reported for bulk material due to size effect.
- Twinning growth mechanisms at the micron scale are highly stochastic leading to either strain hardening or softening.
- The twin growth mechanism shifts from an elongation-dominated process to a thickening-dominated process when boundaries are present along the twin growing path. This is mainly caused by the pile-up at the TB of the dislocations generated ahead of the twin tip. The boundary pile-up of dislocations along the twin shear direction induces a local increase of the shear stress ( $\sigma'_{13}$ ) on the twin plane that limits further lengthwise twin growth.
- The nature of the dislocations located ahead of the lenticular twin tip, accommodating the local crystal misfit in this highly strained region, was characterized by HR-EBSD to be mainly of <a> edge type.
- At the micron scale, Mg accommodates plastic deformation through twin and slip activities up to ~11% of tensile strain

without breaking, showing higher ductility than usually reported for bulk materials.

- When two twins interact through their volume (as for grains B and C), no twin-twin crossing mechanism has been observed between the different {10 $\bar{1}$ 2} twin variants at the location of the twin-twin junction, but rather a third twin variant nucleation (grain D).

Mechanical experiments combined with *in situ* HR-EBSD and post-mortem 3D HR-EBSD is a powerful tool to investigate deformation twinning mechanisms at the micron-scale. It can give a strong experimental basis for subsequent TEM investigations and a strong support to the numerous MD simulations carried out for understanding the interplay between slip and twin activities.

Supplementary data to this article can be found online at <https://doi.org/10.1016/j.matdes.2020.109206>.

## Data availability

All data used during the study are available from the corresponding author by request.

## Declaration of Competing Interest

The authors declare that they have no known competing financial interests or personal relationships that could have appeared to influence the work reported in this paper.

## Acknowledgments

The authors acknowledge financial support from the Swiss National Science Foundation (SNSF project numbers 200021\_179011 and 206021\_183328). The authors would like to thank Dr. Cyril Cayron of Laboratory of ThermoMechanical Metallurgy (LMTM) of EPFL in Neuchâtel for the helpful discussions, and the Scientific Center for Optical and Electron Microscopy ScopeM of the Swiss Federal Institute of Technology ETHZ. SzK and TEJE were supported by the EMPAPOSTDOCS-II program that has received funding from the European Union's Horizon 2020 research and innovation program under the Marie Skłodowska-Curie grant agreement number 754364.

## Appendix A. Stages of deformation during *in situ* EBSD acquisition of Tb1 and Tb2

Table A.1

<i>In situ</i> EBSD acquisition	Tbar 1	Tbar 2
Map 1	$\varepsilon = 0\%$	$\varepsilon = 0\%$
Map 2	$\varepsilon = 2.3\%$	$\varepsilon = 0.7\%$
Map 3	$\varepsilon = 4.7\%$	$\varepsilon = 4.7\%$
Map 4	$\varepsilon = 9.1\%$	$\varepsilon = 6.4\%$
Map 5	$\varepsilon = 11.2\%$	$\varepsilon = 8.8\%$
Map 6	Unloaded	Unloaded

## Appendix B. Nye tensor components

To understand the available terms of  $\alpha$  that arise from EBSD methods on a single surface, the Nye GND density tensor is expressed in terms of the individual elastic strain tensor  $\varepsilon$  and lattice rotation tensor  $\omega$  derivatives, obtained by considering that the distortion tensor  $\beta = I + \varepsilon + \omega$  and that  $\alpha = \nabla \times \beta$ , with  $I$  as the identity matrix. Only the third column of the tensor can be experimentally assessed, because the other elements require derivation in the z direction, perpendicular to the surface.

For completeness,  $\alpha_{sq} = (\alpha_{13}^2 + \alpha_{23}^2 + \alpha_{33}^2)^{1/2}$ . The importance of  $\alpha_{sq}$  is that it does not rely on CrossCourt's L1 optimization method.  $\alpha_{sq}$  relies on the experimentally available three components, and it is proportional to the GND density; therefore by plotting this value we can ensure that what the GND maps generated by CrossCourt report is not an artifact from the minimization estimation.

Fig. 10 c illustrates the  $\alpha_{13}$  magnitude legend referred to the x-y-z global reference frame. For example, an edge dislocation with Burgers vector pointing in the left side hemisphere appears red in the  $\alpha_{13}$  map since it has a component along the x-axis. The same dislocation appears red (or blue) in the  $\alpha_{23}$  map (Fig. 10d) if it has a component in the south (or north) hemisphere. The magnitudes are proportional to the GND density related to different types of dislocations ( $\alpha_{13}$  and  $\alpha_{23}$ : edge type,  $\alpha_{33}$ : screw type).

## References

- [1] B.C. Suh, M.S. Shim, K.S. Shin, N.J. Kim, Current issues in magnesium sheet alloys: where do we go from here? *Scr. Mater.* 84–85 (2014) 1–6, <https://doi.org/10.1016/j.scriptamat.2014.04.017>.
- [2] S.R. Agnew, J.F. Nie, Preface to the viewpoint set on: the current state of magnesium alloy science and technology, *Scr. Mater.* 63 (2010) 671–673, <https://doi.org/10.1016/j.scriptamat.2010.06.029>.
- [3] M. Lentz, M. Risse, N. Schaefer, W. Reimers, I.J. Beyerlein, Strength and ductility with {1011}–{1012} double twinning in a magnesium alloy, *Nat. Commun.* 7 (2016) 1–7, <https://doi.org/10.1038/ncomms11068>.
- [4] Z. Wu, W.A. Curtin, The origins of high hardening and low ductility in magnesium, *Nature*. 526 (2015) 62–67, <https://doi.org/10.1038/nature15364>.
- [5] J.W. Christian, S. Mahajan, Deformation twinning, *Prog. Mater. Sci.* 39 (1995) 1–157, [https://doi.org/10.1016/0079-6425\(94\)00007-7](https://doi.org/10.1016/0079-6425(94)00007-7).
- [6] M.H. Yoo, J.K. Lee, Deformation twinning in h.c.p. metals and alloys, *Philos. Mag. A Phys. Condens. Matter. Struct. Defects Mech. Prop.* 63 (1991) 987–1000, <https://doi.org/10.1080/01418619108213931>.
- [7] E.W. Kelley, J.W.F. Hosford, Plane strain compression of magnesium and magnesium alloy crystals, *Metall. Soc. Am. Inst. Mining, Metall. Pet. Eng. – Trans.* 242 (1968) 5–13.
- [8] M.R. Barnett, Twinning and the ductility of magnesium alloys. Part I: “Tension” twins, *Mater. Sci. Eng. A*. 464 (2007) 1–7, <https://doi.org/10.1016/j.msea.2006.12.037>.
- [9] I.J. Beyerlein, R.J. McCabe, C.N. Tomé, Stochastic processes of {1012} deformation twinning in hexagonal close-packed polycrystalline zirconium and magnesium, *Int. J. Multiscale Comput. Eng.* 9 (2011) 459–480, <https://doi.org/10.1615/IntJMultCompEng.v9.i4.80>.
- [10] M.R. Barnett, Twinning and the ductility of magnesium alloys. Part II. “Contraction” twins, *Mater. Sci. Eng. A*. 464 (2007) 8–16, <https://doi.org/10.1016/j.msea.2007.02.109>.
- [11] M.R. Barnett, A Taylor model based description of the proof stress of magnesium AZ31 during hot working, *Metall. Mater. Trans. A Phys. Metall. Mater. Sci.* 34 (A) (2003) 1799–1806, <https://doi.org/10.1007/s11661-003-0146-5>.
- [12] J. Jeong, M. Alfreider, R. Konetschnik, D. Kiener, S.H. Oh, In-situ TEM observation of {1012} twin-dominated deformation of mg pillars: twinning mechanism, size effects and rate dependency, *Acta Mater.* 158 (2018) 407–421, <https://doi.org/10.1016/j.actamat.2018.07.027>.
- [13] Y.T. Zhu, X.Z. Liao, X.L. Wu, J. Narayan, Grain size effect on deformation twinning and detwinning, *J. Mater. Sci.* (2013) 4467–4475, <https://doi.org/10.1007/s10853-013-7140-0>.
- [14] Q. Yu, Z.W. Shan, J. Li, X. Huang, L. Xiao, J. Sun, E. Ma, Strong crystal size effect on deformation twinning, *Nature*. 463 (2010) 335–338, <https://doi.org/10.1038/nature08692>.
- [15] Q. Yu, L. Qi, K. Chen, R.K. Mishra, J. Li, A.M. Minor, The nanostructured origin of deformation twinning, *Nano Lett.* 12 (2012) 887–892, <https://doi.org/10.1021/nl203937t>.
- [16] X.L. Wu, Y.T. Zhu, Inverse grain-size effect on twinning in nanocrystalline Ni, *Phys. Rev. Lett.* 101 (2008) <https://doi.org/10.1103/PhysRevLett.101.025503>.
- [17] G.S. Kim, Small Volume Investigation of Slip and Twinning in Magnesium Single Crystals, Université de Grenoble, 2011.
- [18] J.R. Greer, J.T.M. De Hosson, Plasticity in small-sized metallic systems: Intrinsic versus extrinsic size effect, *Prog. Mater. Sci.* 2011, pp. 654–724, <https://doi.org/10.1016/j.pmatsci.2011.01.005>.
- [19] G.D. Sim, G. Kim, S. Lavenstein, M.H. Hamza, H. Fan, J.A. El-Awady, Anomalous hardening in magnesium driven by a size-dependent transition in deformation modes, *Acta Mater.* 144 (2018) 11–20, <https://doi.org/10.1016/j.actamat.2017.10.033>.
- [20] H. Feng, Q.H. Fang, B. Liu, Y. Liu, Y.W. Liu, P.H. Wen, Nucleation and growth mechanisms of nanoscale deformation twins in hexagonal-close-packed metal magnesium, *Mech. Mater.* 109 (2017) 26–33, <https://doi.org/10.1016/j.mechmat.2017.03.015>.
- [21] Y.T. Zhu, X.Z. Liao, X.L. Wu, Deformation twinning in nanocrystalline materials, *Prog. Mater. Sci.* 57 (2012) 1–62, <https://doi.org/10.1016/j.pmatsci.2011.05.001>.
- [22] M. Chen, E. Ma, K.J. Hemker, H. Sheng, Y. Wang, X. Cheng, Deformation twinning in nanocrystalline aluminum, *Science* (80-. ) 300 (2003) 1275–1277, <https://doi.org/10.1126/science.1083727>.
- [23] C.M. Byer, B. Li, B. Cao, K.T. Ramesh, Microcompression of single-crystal magnesium, *Scr. Mater.* 62 (2010) 536–539, <https://doi.org/10.1016/j.scriptamat.2009.12.017>.
- [24] E. Lilleodden, Microcompression study of mg (0001) single crystal, *Scr. Mater.* 62 (2010) 532–535, <https://doi.org/10.1016/j.scriptamat.2009.12.048>.
- [25] K.E. Prasad, K. Rajesh, U. Ramamurty, Micropillar and macropillar compression responses of magnesium single crystals oriented for single slip or extension twinning, *Acta Mater.* 65 (2014) 316–325, <https://doi.org/10.1016/j.actamat.2013.10.073>.
- [26] J. Wang, R.G. Hoagland, J.P. Hirth, L. Capolungo, I.J. Beyerlein, C.N. Tomé, Nucleation of a (over{1}1) 0 1 2 twin in hexagonal close-packed crystals, *Scr. Mater.* 61 (2009) 903–906, <https://doi.org/10.1016/j.scriptamat.2009.07.028>.
- [27] L. Capolungo, I.J. Beyerlein, Nucleation and stability of twins in hcp metals, *Phys. Rev. B - Condens. Matter Mater. Phys.* 78 (2008) 1–19, <https://doi.org/10.1103/PhysRevB.78.024117>.
- [28] J. Wang, I.J. Beyerlein, C.N. Tomé, Reactions of lattice dislocations with grain boundaries in mg: implications on the micro scale from atomic-scale calculations, *Int. J. Plast.* 56 (2014) 156–172, <https://doi.org/10.1016/j.ijplas.2013.11.009>.
- [29] M.H. Liang, D.J. Bacon, Computer simulation of dislocation cores in h.c.p. metals II. Core structure in unstressed crystals, *Philos. Mag. A Phys. Condens. Matter. Struct. Defects Mech. Prop.* 53 (1986) 181–204, <https://doi.org/10.1080/01418618608242820>.
- [30] A. Serra, D.J. Bacon, Modelling the motion of {1 1 2} twinning dislocations in the HCP metals, *Mater. Sci. Eng. A* 400–401 (2005) 496–498, <https://doi.org/10.1016/j.msea.2005.01.067>.
- [31] C. Cayron, Hard-sphere displacive model of extension twinning in magnesium, *Mater. Des.* 119 (2017) 361–375, <https://doi.org/10.1016/j.matdes.2017.01.047>.
- [32] B. Syed, J. Geng, R.K. Mishra, K.S. Kumar, [0001] Compression response at room temperature of single-crystal magnesium, *Scr. Mater.* 67 (2012) 700–703, <https://doi.org/10.1016/j.scriptamat.2012.06.036>.
- [33] D. Kiener, W. Grosinger, G. Dehm, R. Pippan, A further step towards an understanding of size-dependent crystal plasticity: in situ tension experiments of miniaturized single-crystal copper samples, *Acta Mater.* 56 (2008) 580–592, <https://doi.org/10.1016/j.actamat.2007.10.015>.
- [34] Y. Liu, N. Li, S. Shao, M. Gong, J. Wang, R.J. McCabe, Y. Jiang, C.N. Tomé, Characterizing the boundary lateral to the shear direction of deformation twins in magnesium, *Nat. Commun.* 7 (2016) <https://doi.org/10.1038/ncomms11577>.
- [35] A. Serra, D.J. Bacon, R.C. Pond, Dislocations in interfaces in the h.c.p. metals - I. Defects formed by absorption of crystal dislocations, *Acta Mater.* 47 (1999) 1425–1439, [https://doi.org/10.1016/S1359-6454\(99\)00016-6](https://doi.org/10.1016/S1359-6454(99)00016-6).
- [36] J. Tu, X. Zhang, J. Wang, Q. Sun, Q. Liu, C.N. Tomé, Structural characterization of {1012} twin boundaries in cobalt, *Appl. Phys. Lett.* 103 (2013) <https://doi.org/10.1063/1.4817180>.
- [37] J. Wang, L. Liu, C.N. Tomé, S.X. Mao, S.K. Gong, Twinning and de-twinning via glide and climb of twinning dislocations along serrated coherent twin boundaries in hexagonal-close-packed metals, *Mater. Res. Lett.* 1 (2013) 81–88, <https://doi.org/10.1080/21663831.2013.779601>.
- [38] M. Gong, J.P. Hirth, Y. Liu, Y. Shen, J. Wang, Interface structures and twinning mechanisms of twins in hexagonal metals, *Mater. Res. Lett.* 5 (2017) 449–464, <https://doi.org/10.1080/21663831.2017.1336496>.
- [39] I.J. Beyerlein, X. Zhang, A. Misra, Growth twins and deformation twins in metals, *Annu. Rev. Mater. Res.* 44 (2014) 329–363, <https://doi.org/10.1146/annurev-matsci-070813-113304>.
- [40] M. Gong, G. Liu, J. Wang, L. Capolungo, C.N. Tomé, Atomistic simulations of interaction between basal <a> dislocations and three-dimensional twins in magnesium, *Acta Mater.* 155 (2018) 187–198, <https://doi.org/10.1016/j.actamat.2018.05.066>.
- [41] A. Fernández, A. Jérusalem, I. Gutiérrez-Urrutia, M.T. Pérez-Prado, Three-dimensional investigation of grain boundary-twin interactions in a mg AZ31 alloy by electron backscatter diffraction and continuum modeling, *Acta Mater.* 61 (2013) 7679–7692, <https://doi.org/10.1016/j.actamat.2013.09.005>.
- [42] S. Xu, L.S. Toth, C. Schuman, J.S. Lecomte, M.R. Barnett, Dislocation mediated variant selection for secondary twinning in compression of pure titanium, *Acta Mater.* 124 (2017) 59–70, <https://doi.org/10.1016/j.actamat.2016.10.063>.
- [43] Y. Pei, A. Godfrey, J. Jiang, Y.B. Zhang, W. Liu, Q. Liu, Extension twin variant selection during uniaxial compression of a magnesium alloy, *Mater. Sci. Eng. A* 550 (2012) 138–145, <https://doi.org/10.1016/j.msea.2012.04.046>.
- [44] Q. Yu, J. Wang, Y. Jiang, R.J. McCabe, N. Li, C.N. Tomé, Twin-twin interactions in magnesium, *Acta Mater.* 77 (2014) 28–42, <https://doi.org/10.1016/j.actamat.2014.05.030>.
- [45] M. Arul Kumar, M. Gong, I.J. Beyerlein, J. Wang, C.N. Tomé, Role of local stresses on co-zone twin-twin junction formation in HCP magnesium, *Acta Mater.* 168 (2019) 353–361, <https://doi.org/10.1016/j.actamat.2019.02.037>.
- [46] J. Ast, G. Mohanty, Y. Guo, J. Michler, X. Maeder, In situ micromechanical testing of tungsten micro-cantilevers using HR-EBSD for the assessment of deformation evolution, *Mater. Des.* 117 (2017) 265–266, <https://doi.org/10.1016/j.matdes.2016.12.052>.
- [47] J. Ast, M.N. Polyakov, G. Mohanty, J. Michler, X. Maeder, Interplay of stresses, plasticity at crack tips and small sample dimensions revealed by in-situ microcantilever tests in tungsten, *Mater. Sci. Eng. A* 710 (2018) 400–412, <https://doi.org/10.1016/j.msea.2017.10.096>.
- [48] C. Niederberger, W.M. Mook, X. Maeder, J. Michler, In situ electron backscatter diffraction (EBSD) during the compression of micropillars, *Mater. Sci. Eng. A* 527 (2010) 4306–4311, <https://doi.org/10.1016/j.msea.2010.03.055>.



- [49] S. Wang, S. Kalácska, X. Maeder, J. Michler, F. Giuliani, T. Ben Britton, The effect of  $\delta$ -hydride on the micromechanical deformation of a Zr alloy studied by in situ high angular resolution electron backscatter diffraction, *Scr. Mater.* 173 (2019) 101–105, <https://doi.org/10.1016/j.scriptamat.2019.08.006>.
- [50] D. Casari, L. Pethő, P. Schürch, X. Maeder, L. Philippe, J. Michler, P. Zysset, J. Schwiedrzik, A self-aligning microtensile setup: application to single-crystal GaAs microscale tension-compression asymmetry, *J. Mater. Res.* 34 (2019) 2517–2534, <https://doi.org/10.1557/jmr.2019.183>.
- [51] Y. Guo, J. Schwiedrzik, J. Michler, X. Maeder, On the nucleation and growth of {112} twin in commercial purity titanium: in situ investigation of the local stress field and dislocation density distribution, *Acta Mater.* 120 (2016) 292–301, <https://doi.org/10.1016/j.actamat.2016.08.073>.
- [52] T.R. Long, C.S. Smith, Single-crystal elastic constants of magnesium and magnesium alloys, *Acta Metall.* 5 (1957) 200–207, [https://doi.org/10.1016/0001-6160\(57\)90166-9](https://doi.org/10.1016/0001-6160(57)90166-9).
- [53] A.J. Wilkinson, G. Meaden, D.J. Dingley, High-resolution elastic strain measurement from electron backscatter diffraction patterns: new levels of sensitivity, *Ultramicroscopy*. 106 (2006) 307–313, <https://doi.org/10.1016/j.ultramic.2005.10.001>.
- [54] A.J. Wilkinson, D. Randman, Determination of elastic strain fields and geometrically necessary dislocation distributions near nanoindentations using electron back scatter diffraction, *Philos. Mag.* 90 (2010) 1159–1177, <https://doi.org/10.1080/14786430903304145>.
- [55] A.J. Wilkinson, T. Ben Britton, Strains, planes, and EBSD in materials science, *Mater. Today* 15 (2012) 366–376, [https://doi.org/10.1016/S1369-7021\(12\)70163-3](https://doi.org/10.1016/S1369-7021(12)70163-3).
- [56] S. Kalácska, Z. Dankházi, G. Zilahi, X. Maeder, J. Michler, P.D. Ispánovity, I. Groma, Investigation of geometrically necessary dislocation structures in compressed Cu micropillars by 3-dimensional HR-EBSD, *Mater. Sci. Eng. A* 770 (2020) <https://doi.org/10.1016/j.msea.2019.138499>.
- [57] R.E. Reed-Hill, W.D. Robertson, Deformation of magnesium single crystals by nonbasal slip, *Jom.* 9 (1957) 496–502, <https://doi.org/10.1007/bf03397907>.
- [58] H. Tonda, K. Nakamura, K. Takashima, {1122}{1123} slip in magnesium single crystal, *J. Japan Inst. Light Met.* 42 (1992) 765–771, <https://doi.org/10.2464/jilm.42.765>.
- [59] H. Conrad, W.D. Robertson, Effect of temperature on the flow stress and strain-hardening coefficient of magnesium single crystals, *Jom.* 9 (1957) 503–512, <https://doi.org/10.1007/bf03397908>.
- [60] O. Bauer, O. Vollenbruck, G. Schikorr, E. Schmid, W. Boas, P. Beck, M. Polanyi, G. Wassermann, W. Fahrenhorst, G. Siebel, W. Stenzel, J. Weerts, K. Weißenberger, E. Goens, G. Sachs, E. Schmid, Beiträge zur Physik und Metallographie des Magnesiums, *Mitteilungen Der Dtsch. Mater* 1932, pp. 16–25, [https://doi.org/10.1007/978-3-642-92044-8\\_2](https://doi.org/10.1007/978-3-642-92044-8_2).
- [61] A.J. Schwartz, M. Kumar, B.L. Adams, D.P. Field, Electron backscatter diffraction in materials science (2009) <https://doi.org/10.1007/978-0-387-88136-2>.
- [62] D. Zhang, L. Jiang, B. Zheng, J.M. Schoenung, S. Mahajan, E.J. Lavernia, I.J. Beyerlein, J.M. Schoenung, E.J. Lavernia, Deformation Twinning (Update), in: *Ref. Modul. Mater. Sci. Mater. Eng.* (2016) <https://doi.org/10.1016/b978-0-12-803581-8.02878-2>.
- [63] S. Mendelson, Dislocation dissociations in hcp metals, *J. Appl. Phys.* 41 (1970) 1893–1910, <https://doi.org/10.1063/1.1659139>.
- [64] F. Wang, S.R. Agnew, Dislocation transmutation by tension twinning in magnesium alloy AZ31, *Int. J. Plast.* 81 (2016) 63–86, <https://doi.org/10.1016/j.jiplas.2016.01.012>.
- [65] A. Serra, D.J. Bacon, Computer simulation of screw dislocation interactions with twin boundaries in H.C.P. metals, *Acta Metall. Mater.* 43 (1995) 4465–4481, [https://doi.org/10.1016/0956-7151\(95\)00128-1](https://doi.org/10.1016/0956-7151(95)00128-1).
- [66] H. Fan, S. Aubry, A. Arsenlis, J.A. El-Awady, The role of twinning deformation on the hardening response of polycrystalline magnesium from discrete dislocation dynamics simulations, *Acta Mater.* 92 (2015) 126–139, <https://doi.org/10.1016/j.actamat.2015.03.039>.
- [67] M.S. Hooshmand, M.J. Mills, M. Ghazisaeidi, Atomistic modeling of dislocation interactions with twin boundaries in Ti, *Model. Simul. Mater. Sci. Eng.* 25 (2017) <https://doi.org/10.1088/1361-651X/aa6323>.
- [68] M. Yuasa, K. Masunaga, M. Mabuchi, Y. Chino, Interaction mechanisms of screw dislocations with {1011} and {1012} twin boundaries in mg, *Philos. Mag.* 94 (2014) 285–305, <https://doi.org/10.1080/14786435.2013.853136>.
- [69] K.D. Molodov, T. Al-Samman, D.A. Molodov, Profuse slip transmission across twin boundaries in magnesium, *Acta Mater.* 124 (2017) 397–409, <https://doi.org/10.1016/j.actamat.2016.11.022>.
- [70] S.R. Kalidindi, A.A. Salem, R.D. Doherty, Role of deformation twinning on strain hardening in cubic and hexagonal polycrystalline metals, *Adv. Eng. Mater.* 5 (2003) 229–232, <https://doi.org/10.1002/adem.200300320>.
- [71] M. Knezevic, A. Levinson, H. Harris, R.K. Mishra, R.D. Doherty, S.R. Kalidindi, Deformation twinning in AZ31: influence on strain hardening and texture evolution, *Acta Mater.* 58 (2010) 6230–6242, <https://doi.org/10.1016/j.actamat.2010.07.041>.
- [72] B. Wang, R. Xin, G. Huang, Q. Liu, Effect of crystal orientation on the mechanical properties and strain hardening behavior of magnesium alloy AZ31 during uniaxial compression, *Mater. Sci. Eng. A* 534 (2012) 588–593, <https://doi.org/10.1016/j.msea.2011.12.013>.
- [73] Y. Xin, L. Lv, H. Chen, C. He, H. Yu, Q. Liu, Effect of dislocation-twin boundary interaction on deformation by twin boundary migration, *Mater. Sci. Eng. A* 662 (2016) 95–99, <https://doi.org/10.1016/j.msea.2016.03.061>.
- [74] A. Serra, D.J. Bacon, R.C. Pond, Twins as barriers to basal slip in hexagonal-close-packed metals, *Metall. Mater. Trans. A Phys. Metall. Mater. Sci.* 33 (2002) 809–812, <https://doi.org/10.1007/s11661-002-0149-7>.
- [75] G. Proust, C.N. Tomé, A. Jain, S.R. Agnew, Modeling the effect of twinning and detwinning during strain-path changes of magnesium alloy AZ31, *Int. J. Plast.* 25 (2009) 861–880, <https://doi.org/10.1016/j.jiplas.2008.05.005>.
- [76] N. Chandra, P. Dang, Atomistic simulation of grain boundary sliding and migration, *J. Mater. Sci.* 34 (1999) 655–666, <https://doi.org/10.1023/A:1004531706998>.
- [77] S.-H. Kim, J.-H. Park, H.-K. Kim, J.-P. Ahn, D.-M. Whang, J.-C. Lee, Twin boundary sliding in single crystalline Cu and Al nanowires, *SSRN Electron. J.* (2020) <https://doi.org/10.2139/ssrn.3513123>.
- [78] Y. Yue, Q. Zhang, X. Zhang, Z. Yang, P. Yin, L. Guo, In Situ Observation of Twin Boundary Sliding in Single Crystalline Cu Nanowires, *Small*, 2017 <https://doi.org/10.1002/sml.201604296>.
- [79] K. Konopka, J. Mizera, J.W. Wyrzykowski, Generation of dislocations from twin boundaries and its effect upon the flow stresses in FCC metals, *J. Mater. Process. Technol.* 99 (2000) 255–259, [https://doi.org/10.1016/S0924-0136\(99\)00434-3](https://doi.org/10.1016/S0924-0136(99)00434-3).
- [80] R. Namakian, G.Z. Voyiadjis, P. Kwaśniak, On the slip and twinning mechanisms on first order pyramidal plane of magnesium: Molecular dynamics simulations and first principal studies, *Mater. Des.* 191 (2020) <https://doi.org/10.1016/j.matdes.2020.108648>.
- [81] M. Ghazisaeidi, W.A. Curtin, Analysis of dissociation of {c} and {c + a} dislocations to nucleate {1 0 1 2} twins in mg, *Model. Simul. Mater. Sci. Eng.* 21 (2013) 0–13, <https://doi.org/10.1088/0965-0393/21/5/055007>.
- [82] J. Wang, I.J. Beyerlein, J.P. Hirth, Nucleation of elementary {1011} and {1013} twinning dislocations at a twin boundary in hexagonal close-packed crystals, *Model. Simul. Mater. Sci. Eng.* 20 (2012) <https://doi.org/10.1088/0965-0393/20/2/024001>.
- [83] J. Wang, Q. Yu, Y. Jiang, I.J. Beyerlein, Twinning-associated boundaries in hexagonal close-packed metals, *Jom.* 66 (2014) 95–101, <https://doi.org/10.1007/s11837-013-0803-0>.
- [84] J. Wang, I.J. Beyerlein, C.N. Tomé, An atomic and probabilistic perspective on twin nucleation in mg, *Scr. Mater.* 63 (2010) 741–746, <https://doi.org/10.1016/j.scriptamat.2010.01.047>.
- [85] F. Wang, C.D. Barrett, R.J. McCabe, H. El Kadiri, L. Capolungo, S.R. Agnew, Dislocation induced twin growth and formation of basal stacking faults in {1012} twins in pure mg, *Acta Mater.* 165 (2019) 471–485, <https://doi.org/10.1016/j.actamat.2018.12.003>.
- [86] H. El Kadiri, C.D. Barrett, J. Wang, C.N. Tomé, Why are {1 0 1 2} twins profuse in magnesium? *Acta Mater.* 85 (2015) 354–361, <https://doi.org/10.1016/j.actamat.2014.11.033>.
- [87] A. Serra, D.J. Bacon, A new model for {1012} twin growth in hcp metals, *Philos. Mag. A Phys. Condens. Matter. Struct. Defects Mech. Prop.* 73 (1996) 333–343, <https://doi.org/10.1080/01418619608244386>.
- [88] A. Serra, D.J. Bacon, Interaction of a moving {1012} twin boundary with perfect dislocations and loops in a hcp metal, *Philos. Mag.* 90 (2010) 845–861, <https://doi.org/10.1080/14786430903023901>.
- [89] X. Wang, P. Mao, Z. Liu, Z. Wang, F. Wang, L. Zhou, Z. Wei, Nucleation and growth analysis of {101 2} extension twins in AZ31 magnesium alloy during in-situ tension, *J. Alloys Compd.* 817 (2020) <https://doi.org/10.1016/j.jallcom.2019.152967>.
- [90] S.H. Oh, M. Legros, D. Kiener, G. Dehm, In situ observation of dislocation nucleation and escape in a submicrometre aluminium single crystal, *Nat. Mater.* 8 (2009) 95–100, <https://doi.org/10.1038/nmat2370>.
- [91] K. Kang, J. Wang, I.J. Beyerlein, Atomic structure variations of mechanically stable fcc-bcc interfaces, *J. Appl. Phys.* 111 (2012) <https://doi.org/10.1063/1.3693015>.
- [92] J.P. Hirth, R.C. Pond, R.G. Hoagland, X.Y. Liu, J. Wang, Interface defects, reference spaces and the Frank-Bilby equation, *Prog. Mater. Sci.* 58 (2013) 749–823, <https://doi.org/10.1016/j.pmatsci.2012.10.002>.
- [93] J. Wang, J.P. Hirth, R.C. Pond, J.M. Howe, Rotational partitioning at two-phase interfaces, *Acta Mater.* 59 (2011) 241–251, <https://doi.org/10.1016/j.actamat.2010.09.028>.
- [94] S. Vaidya, S. Mahajan, ACCOMMODATION AND FORMATION OF left brace 112 OVER BAR 1 right brace TWINS IN Co SINGLE CRYSTALS, *Acta Metall.* 28 (1980) 1123–1131, [https://doi.org/10.1016/0001-6160\(80\)90095-4](https://doi.org/10.1016/0001-6160(80)90095-4).
- [95] S. Mahajan, Twin-slip and twin-twin interactions in Mo-35 at. % re alloy, *Philos. Mag.* 23 (1971) 781–794, <https://doi.org/10.1080/14786437108216988>.
- [96] C.C. Aydiner, J.V. Bernier, B. Clausen, U. Lienert, C.N. Tomé, D.W. Brown, Evolution of stress in individual grains and twins in a magnesium alloy aggregate, *Phys. Rev. B - Condens. Matter Mater. Phys.* 80 (2009) 1–6, <https://doi.org/10.1103/PhysRevB.80.024113>.
- [97] M. Arul Kumar, I.J. Beyerlein, C.N. Tomé, Effect of local stress fields on twin characteristics in HCP metals, *Acta Mater.* 116 (2016) 143–154, <https://doi.org/10.1016/j.actamat.2016.06.042>.
- [98] L. Balogh, S.R. Niezgoda, A.K. Kanjarla, D.W. Brown, B. Clausen, W. Liu, C.N. Tomé, Spatially resolved in situ strain measurements from an interior twinned grain in bulk polycrystalline AZ31 alloy, *Acta Mater.* 61 (2013) 3612–3620, <https://doi.org/10.1016/j.actamat.2013.02.048>.
- [99] Y. Guo, H. Abdolvand, T.B. Britton, A.J. Wilkinson, Growth of {1122} twins in titanium: a combined experimental and modelling investigation of the local state of deformation, *Acta Mater.* 126 (2017) 221–235, <https://doi.org/10.1016/j.actamat.2016.12.066>.
- [100] S. Niknejad, S. Esmaeili, N.Y. Zhou, The role of double twinning on transgranular fracture in magnesium AZ61 in a localized stress field, *Acta Mater.* 102 (2016) 1–16, <https://doi.org/10.1016/j.actamat.2015.09.026>.
- [101] M. Arul Kumar, A.K. Kanjarla, S.R. Niezgoda, R.A. Lebensohn, C.N. Tomé, Numerical study of the stress state of a deformation twin in magnesium, *Acta Mater.* 84 (2015) 349–358, <https://doi.org/10.1016/j.actamat.2014.10.048>.